 doi:10.20944/preprints202012.0025.v1

Article

Transport of Gaseous Hydrogen Peroxide and Ozone into Bulk Water vs. Electrosprayed Aerosol

Mostafa Elsayed Hassan, Mário Janda and Zdenko Machala *

Division of Environmental Physics, Faculty of Mathematics, Physics and Informatics, Comenius University, Mlynská Dolina, 842 48 Bratislava, Slovakia
mostafa.hassan@fmph.uniba.sk
* Correspondence: ZM machala@fmph.uniba.sk; MJ mario.janda@fmph.uniba.sk

Abstract: Production and transport of reactive species through plasma-liquid interactions plays a significant role in multiple applications in biomedicine, environment, and agriculture. We experimentally investigated the transport mechanisms of hydrogen peroxide H_2O_2 and ozone O_3, as the typical plasma species, into water. We measured the solvation of gaseous H_2O_2 and O_3 in airflow into water bulk vs. electrosprayed microdroplets while changing the gas and water flow rates, applied voltage that determines the gas-liquid interface area, and treatment time. The solvation rate of H_2O_2 and O_3 increased with the treatment time and the gas-liquid interface area. The total surface area of the electrosprayed microdroplets was larger than that of the bulk, but their lifetime was much shorter. We estimated that only microdroplets with diameters below ~ 40 μm could achieve the saturation by O_3 during their lifetime, while the saturation by H_2O_2 was impossible due to its depletion from air. Besides the short-lived flying microdroplets, the longer-lived bottom microdroplets substantially contributed to H_2O_2 and O_3 solvation in water electrospray. This study contributes to a better understanding of the gaseous H_2O_2 and O_3 transport into water as a function of different parameters and will lead to design optimization of the plasma-liquid interaction systems.

Keywords: plasma-liquid interactions; water electrospray; aerosol microdroplet; bulk water, plasma-activated water; Henry's law solubility; ozone; hydrogen peroxide

1. Introduction

Interactions of non-equilibrium plasmas with liquids, known as plasma-liquid interactions [1–3], have become an emerging topic in the field of plasma science and technology which contributed to many applications, ranging from environmental remediation [4,5] to material science [6,7] and health care [8,9]. The varieties of plasma interactions with liquids are of great importance in a plethora of various plasma-liquid systems because the liquid properties change in time under the influence of the interaction with plasma, and vice-versa [10]. The distinctive characteristics of non-equilibrium (cold) atmospheric plasmas, which are often created in ambient air, lead to a broad extension of their use in various biomedical applications [11–16]. Cold plasmas can be effective tools for microbial decontamination and sterilization [17], interact with living tissues [18], treat mammalian and cancerous cells [19], induce blood coagulation [17,20], can be applied in wound healing [21] and dentistry [22], and can be successfully transferred into clinical practice [15,16,23]. Novel applications in water cleaning, food production, and agriculture (e.g. seed germination and plant growth promotion, pest control) without causing undesired side-effects or environmental burdens are on their way [24–27].

Atmospheric air plasmas in contact with liquid water or aqueous solutions generate "plasma-activated water" (PAW), which contains various reactive oxygen and nitrogen species (RONS), e.g. hydrogen peroxide (H_2O_2), nitrate (NO_3^-), and nitrite (NO_2^-) anions, ozone (O_3), as well as other short-lived species [24,28–30]. It has been reported by several groups that these typically acidic

 doi:10.20944/preprints202012.0025.v1

PAW solutions are effective in killing and inactivating bacteria in suspensions [29,31,32]. PAW and other plasma-activated water solutions are examples of the outcome of plasma-liquid interaction, where the reactive plasma RONS are transported/dissolved into water. This is very relevant in plasma applications in biomedicine and medical therapies, where the plasma interaction with cells and tissues is usually mediated through thin layers of water solutions covering the biological cells and tissues, and the RONS activate and interact with this liquid thin layer before they reach the tissue [31].

The motivation of this article is to better understand the transport mechanisms of various plasma gaseous reactive species into the water. This would bring a stronger theoretical-experimental baseline for the progressing research of cold plasma and PAW applications in biomedicine: beginning from bio-decontamination to various medical therapies (dentistry, wound healing, cancer treatments), as well as applications in water cleaning, food production, and agriculture.

In general, the transport (solvation, dissolution) of gases into liquids is governed by Henry's law solubility coefficient k_H (mol/m^{3}Pa) which is usually used to describe the solubility of the gas species in liquids, e.g. water, defined as:

$$k_H \stackrel{\text{def}}{=} c_i/p_i, \tag{1}$$

Here, c_i is the molar concentration of i-species in the aqueous phase and p_i is the partial pressure of that species in the gas phase. k_H is described as the proportionality factor of the amount of the dissolved gas in the aqueous phase to its partial pressure in the gas phase. In atmospheric chemistry, these coefficients are important to describe the distribution of trace species between the air and liquid droplets (aerosol). Henry's law coefficient can be also expressed as the dimensionless ratio between the aqueous-phase concentration c_i of a species and its gas-phase concentration c_g in Equation (2), where, R and T are the gas constant and temperature, respectively [33].

$$k_H^{cc} \stackrel{\text{def}}{=} c_i/c_g = k_H \times RT, \tag{2}$$

Hydrogen peroxide H_2O_2 and ozone O_3 as examples of the plasma long-lived gaseous RONS have Henry's law solubility coefficients $k_H \approx 9 \times 10^2$ and 10^{-4} mol/m^{3}Pa, respectively. Henry's law solubility coefficient of H_2O_2 is almost 7 orders of magnitude larger than that of O_3, which means that these RONS generated in the air (gas phase) are not dissolved into water (aqueous phase) at the same rate. While H_2O_2(g) readily transfers into the water through the gas-liquid interface, O_3(g) is hardly dissolved into water based on its very low Henry's law coefficient. Species transport through the gas-liquid interface can be conceptualized by the change in density across the interface and estimates that this transition occurs over a few nanometers or less. The length scale of the transition from the vapor to liquid is 0.3-0.6 nm under ambient conditions. The rough interface has fluctuations over picoseconds with water exchanging from the bulk to the boundary over several picoseconds [3]. The plasma-liquid interface area is a key parameter maximizing the contact between the plasma and the treated water solution, thus determining the obtained plasma chemical effects [34].

Verlackt et al. in a 2D axisymmetric fluid model investigated the accumulation of RONS in a buffered aqueous solution during the plasma jet treatment flowing into the ambient air. The density of H_2O_2 species shows a sudden drop at the gas-liquid interface due to the fast transfer into the liquid, where its density is significantly higher compared to the gas phase. On the other hand, the density of O_3 species remains constant above the gas-liquid interface for 1 min of plasma treatment, where its density is much higher in the gas phase compared to the liquid phase [35].

Water was considered as a model system in MD simulations to provide an atomic-level insight into the plasma-liquid film interaction mechanisms. It was found H_2O_2 species can travel through the water interface layer during the simulation period 1.4 ns, penetrate deeper, and eventually reach the surface of biomolecules. The obtained calculations predict that the main plasma species can interact with bio-organisms [36].

Kruzselnicki et al. in computational modeling from 0 and 2D investigated DBD air plasma activation/treatment of water microdroplets. Long-lived RONS in liquid: e.g. H_2O_2(aq) and O_3(aq)

 doi:10.20944/preprints202012.0025.v1

are relatively stable and accumulate with each discharge pulse. Lower k_H species, such as O_3, quickly reach a saturated state relative to their gas-phase density, while large k_H species continue to increase their aqueous densities. For lower k_H, a droplet is rapidly saturated and "tracks" gas-phase species, while for large k_H, the droplet continues to solvate the gas-phase species. High k_H species take a longer time to reach equilibrium and are more sensitive to transport [37,38].

For aerosol diffusion, the increasing number of droplets leads to an increase in their total volume, their surface area, while the distance between them decreases. The larger surface-to-volume ratio increases the rate of gas-phase solvation into the droplets if the droplet is under-saturated. If the droplet density is too low, solvation is transport-limited (large distances between the droplets) but if the droplet density is too high, depletion of the gaseous density limits the solvation (large total volume of droplets), especially for high k_H species such as H_2O_2 due to their rapid transport into the droplets [37,38].

Oinuma et al. in their quantitative study investigated the reactivity transfer of OH from the gas phase RF discharge plasma to the liquid phase and how its diffusion limitations impact formate decomposition in the water microdroplets. In droplets with a lower diameter, they observed a 50% reduction in formate concentration after plasma treatment for droplet residence times of ~10 ms, while only 28% for droplets with higher diameter. The oxidation of formate by the plasma was improved after plasma treatment of smaller size droplets with increased surface-to-volume ratio [39].

Plasma activation of water droplets and aerosols results in an increasing surface-to-volume ratio and thus accelerates the transport of RONS into the water. This concept has been adopted by several research groups [40–42], as well as our previous work [31,32,43]. For instance, in two different cold air plasma sources (streamer corona and transient spark discharge), PAW was prepared by applying water electrospray to fine aerosol droplets directly through the active plasma zone, which results in a very efficient transfer of gaseous RONS into water. The increased surface area of the plasma-liquid interface promotes water evaporation and the transfer of RONS from the plasma into the water. H_2O_2(g) produced near the air plasma-liquid water interface shows an extremely fast dissolution through this gas-liquid interface [31].

In similar comparative experiments of Bosi et al., the concentrations of O_3 and H_2O_2 produced in two atmospheric plasma discharge sources (streamer and dielectric barrier DBD) were determined for water treatment as a function of input energy. In the solutions treated with the streamer, both O_3 and H_2O_2 were present in higher concentrations than with the DBD. For both configurations, the concentration of O_3 in solution increased at the beginning of the treatment, reached a maximum, and then decreased, while the concentrations of H_2O_2 increased during all the treatment time [44].

In a review by Locke et al., the formation of H_2O_2 was investigated in various electrical discharge plasma reactors with water. Several relatively high energy discharges directly in and over the liquid water with bubbles, and capillary discharges showed improvements in gas-liquid mass transfer characteristics. The highest H_2O_2 yields were found for the water droplet spray which provides large surface areas and small length scales to enhance the mass transfer rates, followed by the water vapor gas [45].

H_2O_2 formation in multiple plasma-water systems has been extensively studied over the last decades. In a study of H_2O_2 formation in hybrid gas-liquid electrical discharge reactors (with different configurations), the corona-like discharge was applied directly above the bulk water surface. The H_2O_2 concentration as a function of time increased almost linearly with the applied voltage and the production rates of H_2O_2 were similar in all reactor configurations [46]. In electrical discharges using different gases (air, argon, and oxygen) over the water surface, the higher efficiency of H_2O_2 formation as a function of power was attributed to the large electric field, and current streamers interacting with the water surface causing an efficient mixing at the interface. Corona discharges in a similar system yield H_2O_2 production very similar to the other gas plasma reactors over water [47].

 doi:10.20944/preprints202012.0025.v1

Winter et al. tracked the plasma generated H_2O_2 from the gas into the liquid phase. With a rising H_2O_2 amount in the gas phase, the liquid phase H_2O_2 concentration increases whether H_2O_2 is created by the plasma in the gas phase or by the H_2O_2 bubbler (without plasma), with a slightly higher liquid H_2O_2 concentration for the plasma case. It was found that more than 60 % of H_2O_2 produced in the liquid phase was without a direct plasma effect. This is because the H_2O_2 solvation process in the gas phase is dominant [48].

Electrospray (ES) or electrohydrodynamic atomization of liquids is one of the very efficient ways of producing liquid aerosols. It occurs from a conical meniscus located at the end of a capillary tube continuously supplied with liquid under the influence of a strong electric field. When a liquid flows through the nozzle (capillary tip) which is exposed to an electric field, positive and negative charges separate inside the liquid droplet, and charges of the same polarity as the nozzle, move towards the droplet surface, inducing a surface charge density on the liquid-air interface (liquid surface). The charged droplets generated from the nozzle of the high electric potential have different sizes ranging from large (mm) to very small (nm) droplets, at various droplet populations from polydisperse to monodisperse, at different flow rates where the droplet diameter (size) is controlled by varying the ES flow rate or the electrical conductivity of the liquid [49–53]. There are many parameters involved in the ES process, which determine different modes of continuous and intermittent ES, producing aerosols of highly varied characteristics. The important parameters are the geometry of the system used, applied voltage, the dielectric strength of the ambient medium, liquid flow rate, and the physical properties of the liquid such as electrical conductivity, surface tension, and viscosity. Due to the high electric potential and low radii of the capillary nozzle, water meniscus, and the jet at the nozzle outlet, the electric field at the surface of those objects is often sufficiently high to cause ionization processes in the surrounding gas. The corona discharge occurs at a low discharge power around the sharp edges of the nozzle where the electric field is locally applied [54]. The time of surviving the liquid aerosol droplets in the sub-micrometer dimension (a few milliseconds) in low-temperature atmospheric pressure (corona) plasmas, is sufficient to produce many chemical reactions in the liquid aerosol [55].

The coupling of plasma-liquid interaction to the liquid ES with plasma chemical processes has many technical advantages, as it employs the same device and the same high voltage power supply applied to the capillary nozzle. Also, as mentioned above, this configuration enables the efficient mass transfer of active species produced by plasma into the water droplets due to the micrometer-scale dimensions of the droplets with a large surface-area-to-volume ratio [56]. The interest and applications of water ES for the liquid sprays have been applied to various areas due to low cost, environment-friendly, and biocompatible water treatment [57].

Stancampiano et al. in their review conclude that plasma-aerosol droplets act as efficient microreactors where reaction rates, mixing and surface-to-volume ratio are enhanced. Ongoing experimental and simulation work in plasma control developments and precision microdroplet generation, which are in turn affected by the range of available gases, liquids, or colloids and the choice of plasma parameters, droplet sizes, and exposure time, as well as a better understanding of droplet transport for the in-situ delivery of chemicals, will lead to opening new horizons for future plasma applications [58].

In this work, we focus on studying the transport mechanism of highly vs. lowly soluble cold air plasma generated species into the water: H_2O_2 vs. O_3. We compare the transport of these species separately, into the bulk water through a simple water surface and into aerosols generated by ES. We measure H_2O_2 and O_3 concentrations dissolved into the water, and their depletion in the gas phase due to this transport according to Henry's law solubility. Changing the water flow rate and the applied voltage on the ES needle electrode is considered a turning point between the lower to the larger surface area of the produced water droplets. This change creates accelerated charged droplets with different specifications such as size, average speed, and lifetime inside the reactor filled with the studied gaseous species. We control these parameters with various gas flow rates of gaseous H_2O_2 and O_3 during different treatment times when the water (bulk or aerosol) is exposed to the incident H_2O_2 and O_3 species. We present experimental results coupled with theoretical

 doi:10.20944/preprints202012.0025.v1

calculations and analyze the solvation saturation coefficients for H_2O_2 and O_3 separately. Our analyses will presumably lead to a deeper understanding of the gaseous plasma species transport into the water (aqueous) phase for various surface-to-volume ratios, which underlines many air plasma applications in biomedicine, environmental sciences, and agriculture.

2. Materials and Methods

The transport of gaseous H_2O_2 and O_3 generated by external sources into water is investigated in two types of reactors: bulk water and electrosprayed (ES) aerosols. The concentration of dissolved H_2O_2 and O_3 in the water and their loss in the gas phase was measured. The optical imaging technique was employed to analyze the size, density, and surface area of the electrosprayed water microdroplets during the transport of H_2O_2 and O_3 from air into water.

2.1. Generation and analysis of H_2O_2 and O_3 in the gas phase

Because of relatively low concentrations of H_2O_2 and O_3 generated by the positive corona discharge that we typically use in biomedical applications [22,31,32,43], we used here two different external gas sources of higher concentrations of H_2O_2 or O_3. It enabled us to study the species transport into the water at higher gaseous concentrations. We worked with H_2O_2 and O_3 gases individually, where each one was mixed separately with an airflow to form a gas mixture with a specific dilution ratio, flow rate, and gas concentration. This gas mixture was pumped into two different reactors (ES and bulk) through PTFE tubes with an inner diameter of 4 mm and then measured by two individual electrochemical gas sensors of H_2O_2 and O_3, type MEMBRAPOR. The gas sensors were connected to the reactor by PTFE and silicon tubes with the same inner diameter. Each gas sensor was attached to its transmitter board connected with an Arduino circuit, where the functional code is uploaded and displayed on LCD showing the gas concentrations in ppm.

The external source for H_2O_2 is a bubbler glass tube containing 30 % (w/w) H_2O_2 solution in water with a corresponding molar concentration of 9.8 M. It is bubbled using a variable airflow to produce H_2O_2 vapor with a high relative humidity > 90 %. This H_2O_2 vapor is mixed by a 1:1 ratio with dry air from an air pump to avoid the condensing of the water vapor in the H_2O_2 gas sensor and to keep a recommended relative humidity range of 15-90 %. The H_2O_2 gas sensor type H_2O_2/CB-500 has a nominal range of 0-500 ppm with a resolution < 1 ppm and maximum overload of 1000 ppm. We run the H_2O_2 experiment at a concentration value of ~ 110 ppm of H_2O_2.

We used the O_3 generator type EASELEC as an external source of O_3 with an O_3 output of 300 mg/h and a flow rate 2-3 l/min, which is mixed by 2:1 ratio with an airflow produced by an air pump to reach a concentration of ~ 450 ppm of O_3 before starting the O_3 experiment. Since the O_3 generator has a constant output flow rate, we used a by-pass valve in one of its two output terminals to avoid limiting its designed gas flow rate and allow a lower concentration of O_3 than its default output. The O_3 gas sensor type O_3/C-1000 has a nominal range of 0-1000 ppm with a resolution of 0.3 ppm and maximum overload of 2000 ppm.

We control the air-flow rate with H_2O_2 vapor or O_3 gas using flow meters AALBORG. During each experiment of H_2O_2 or O_3, the gas sensors are supposed to record a decrease in the H_2O_2 or O_3 concentration of the gas mixture inside the reactor. This concentration loss in the gas phase represents how much of the H_2O_2 or O_3 species were transported/dissolved into the water (bulk or aerosols).

2.2. Transport of gaseous H_2O_2 and O_3 into the bulk water

The experimental setup shown in Figure 1 consists of the air pump, external sources of H_2O_2 vapor and O_3 gases, and gas sensors as described in the previous section.

Preprints (www.preprints.org) | NOT PEER-REVIEWED | Posted: 1 December 2020 doi:10.20944/preprints202012.0025.v1

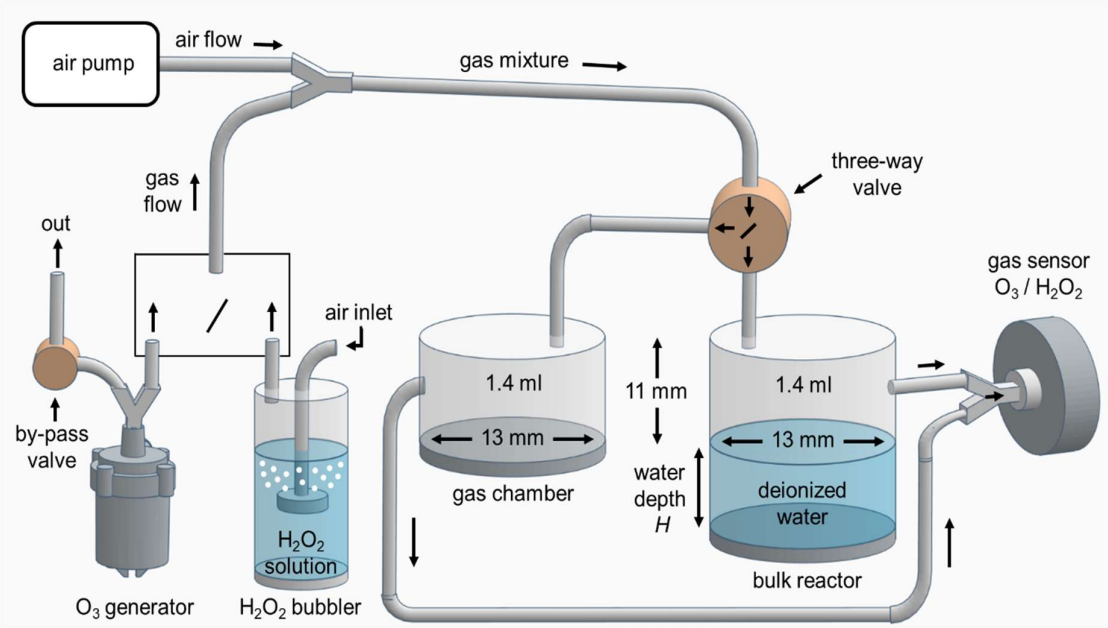

Figure 1. Schematic of the experimental setup for investigation H_2O_2 and O_3 transport into bulk water.

We used in parallel the bulk water reactor and the gas chamber that have the same cylindrical geometry and dimensions (diameter, height, and volume of the gaseous space 13 mm, 11 mm, and 1.4 ml, respectively). There is a piston at the bottom of the bulk reactor to keep the height and volume of the gaseous space constant for different water volumes. The filled bulk of deionized water (with conductivity < 3 μS/cm) at the bottom of the reactor has a fixed surface area exposed to H_2O_2 or O_3 gaseous species. The volume of the bulk water is determined by its depth *H*.

The gas mixture of H_2O_2 diluted vapor or O_3 diluted gas is first pumped through a three-way valve type BUERKLE PP/PE into the gas chamber with no water and then into the gas sensor. When reaching the stable starting point of the gas concentrations 110 or 450 ppm for the H_2O_2 vapor or O_3 gas, respectively, the gas mixture is transferred into the bulk reactor filled with the specific water volume. At that moment, the treatment time is started, and the gas sensor is connected to the bulk reactor. The treatment time means the exposure time of this bulk water (with a fixed surface area and different volumes) to the incoming gas mixture. There was slight turbulence of the surface of the water bulk during the flow of the gas mixture at the highest flow rates used (2 l/min).

2.3. Analysis of the sizes of water microdroplets using Fast/HS camera imaging and transport of gaseous H_2O_2 and O_3 into the water aerosols

We measured the diameter and density of the water aerosol (large droplets + electrosprayed microdroplets) by high-speed visualization to investigate the transport of the gaseous species into the water. Figure 2 shows the schematic diagram of our ES experimental setup. It consists of a positive dc High Voltage (HV) power supply type Spellman's Bertan model 210-30R of 135 W and a syringe pump type NE-300 which delivers the deionized water (with conductivity < 3 μS/cm) continuously through a silicon tube with an inner diameter of 2 mm and controlled water flow rates (100-1000) μl/min into a blunt hollow needle electrode (anode) nozzle with the outer and inner diameters 0.7 and 0.5 mm, respectively. The needle electrode is placed opposite to a rounded wire of 1.5 mm diameter as a grounded electrode (cathode). The two electrodes are in point-to-plane geometry, both are stainless-steel with the shortest gap distance of 16 mm. HV from the power supply is applied through a ballast resistor 13.5 MΩ on the needle electrode. This HV is measured using a dc HV probe type AGILENT N2771A and then processed by a digital oscilloscope type TEKTRONIX TDS 1012.

Preprints (www.preprints.org) | NOT PEER-REVIEWED | Posted: 1 December 2020 doi:10.20944/preprints202012.0025.v1

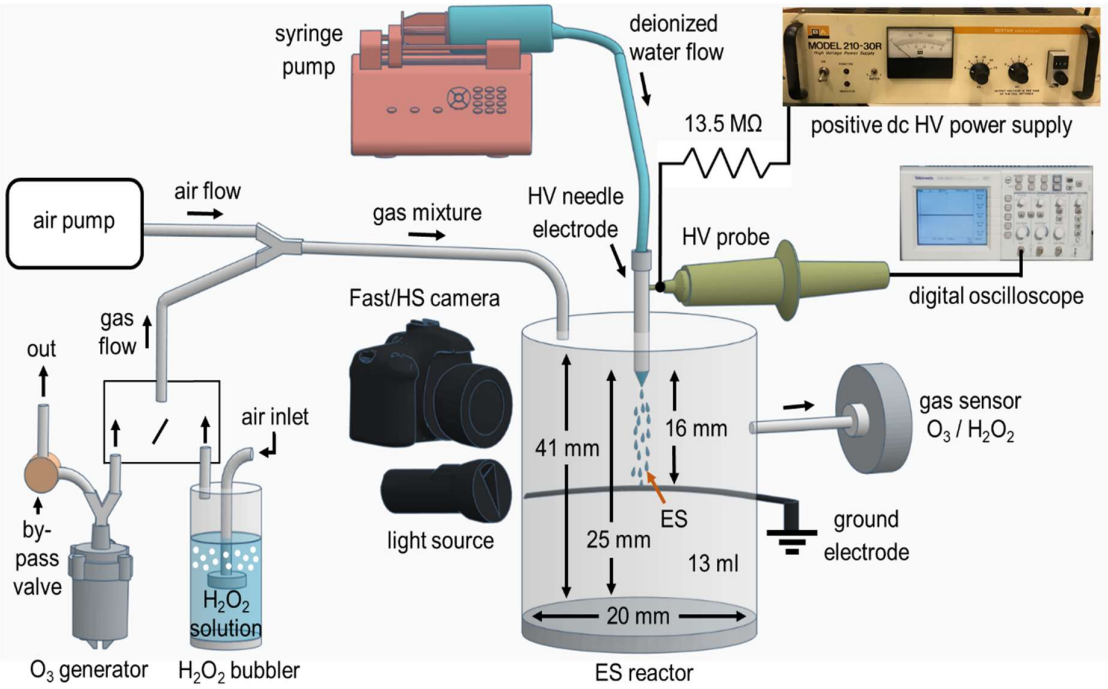

Figure 2. Schematic of the experimental setup for the Fast/HS camera imaging technique and investigation H_2O_2 and O_3 transport into water ES.

We used two types of cameras placed in front of the water aerosols to visualize the electrosprayed aerosol and measure the size of the water droplets. A digital Fast camera type CASIO EXILIM was used mainly for the slower and larger size water droplets, with typical record parameters 60 fps (frame per second) and shutter speed 1/40,000 s (exposure time 25 μs). It provided photographs of size 562 × 623 pixels and resolution 29.2 μm /pixel. Additionally, High Speed (HS) camera Photron FASTCAM SA-Z type 2100K-C-32GB was used mainly for the faster and lower size of the water microdroplets produced during the ES process, with typical record parameters 25,000 fps and shutter speed 1/50,000 s and 1/133,333 s (exposure time 20-7.5 μs) which provided photographs of the size 840 × 1024 pixels and resolution 21.875 μm /pixel.

To improve the spatial resolution of the camera at short exposure times and high shutter speed, sufficient light illumination was needed. The droplets were illuminated with two strong light sources, white LED type LEDLENSER P7R placed in front of the Fast camera with the droplets in between, and type DEDOLIGHT daylight 400D placed beside the HS camera directed to the microdroplets. The Fast/HS camera records photographs of the electrosprayed water microdroplets, which were processed and analyzed by the software Microsoft Office Picture Manager and GIMP (version 2.10.22).

To allow a very efficient mass transfer of the studied species (H_2O_2 and O_3) into water aerosols and to enable the gas analyses and measurements, the HV needle and the ground wire electrodes were enclosed inside a transparent plastic reactor in which the water aerosols (large droplets + ES microdroplets) are produced and collected. It has a cylindrical geometry with the dimensions of diameter, height, and volume of gaseous space: 20 mm, 41 mm, and 13 ml, respectively. The transport process of H_2O_2 and O_3 gaseous species into water aerosols occurs in this gaseous space along with a 25 mm flight distance of the water microdroplets from the needle electrode to the bottom of the reactor. The lifetime of these water microdroplets is the time before they reach the bottom of the ES reactor. There is an adjustable piston at the bottom of the reactor to keep the constant volume of the gaseous space and the flight distance when working with different water flow rates and treatment times.

Before starting the water flow and the applied HV on the needle electrode, the gas mixture of H_2O_2 vapor or O_3 gas diluted with air was pumped into the ES reactor, and the gas sensors were employed for measuring their gas concentration. The H_2O_2 or O_3 experiment started when the gas mixture concentration of H_2O_2 vapor or O_3 gas reached 110 or 450 ppm, respectively. Then the water flow at the specific applied voltage on the needle electrode was started, for a given treatment time. The treatment time is the exposure time of the water aerosols to the gas mixture from the start until the end of the water flow.

2.4. Analysis of H_2O_2 and O_3 in the aqueous phase using UV-vis spectroscopy

The aqueous phase analysis is related to the amount of the gas concentrations of H_2O_2 and O_3 in the gas phase, which are dissolved/transported into the water aerosols and bulk. We used UV-vis spectroscopy colorimetric methods for the chemical analysis of H_2O_2 and O_3 in the aqueous phase. The collected water samples with added chemical reagents were analyzed by a UV/VIS absorption spectrophotometer UV-1800 Shimadzu.

For H_2O_2, we used $TiOSO_4$ (titanium oxysulfate) reagent. H_2O_2 reacts with the titanium (IV) ions under acidic conditions which produced a yellow-colored product of pertitanic acid H_2TiO_4 with the absorption maximum at 407 nm [59]. The concentration of H_2O_2 is proportional to the absorbance according to Lambert-Beer's law (molar extinction coefficient $\varepsilon = 6.89 \times 10^2$ L/mol.cm).

For O_3, we used a simple quantitative colorimetric standardized detection method for the dissolved O_3 in water using the indigo blue reagent II for higher concentrations of O_3 (0.05-0.5 mg/L) [32,60]. O_3 decolorizes the indigo potassium trisulfonate dye rapidly in acidic conditions and the colorless product isatin is formed by the bleaching process. The decrease of the absorbance at 600 nm ($\varepsilon = 2.38 \times 10^4$ L/mol.cm) is linearly proportional to the increase of O_3 concentration. Although this analytical method has limitations in plasma-treated solutions due to cross-correlations with other RONS [61], it can be safely used in this experiment with air containing O_3 only.

3. Results

3.1. Solvation of O_3 and H_2O_2 in bulk water

Figure 3 shows the amount of dissolved O_3 and H_2O_2 into bulk water at various water volumes and treatment (interaction) times. Both O_3 and H_2O_2 solvation depends almost linearly on the treatment time. It is interesting to compare the dissolved molar amounts of O_3 and H_2O_2: while O_3 dissolves at the maximum of 0.9 nmol (gas flow rate 0.8 l/min, interaction time 4 min in Figure 3a), H_2O_2 dissolves up to 10 μmol in Figure 3c at similar conditions. This agrees with a much higher Henry's law coefficient k_H of H_2O_2 compared to O_3, however, the measured difference is 4, not 7 orders of magnitude as one would expect based on the difference of k_H. We will get to this point later (in subsection 4.1). The bulk liquid experiments show that H_2O_2 is very well soluble even without the formation of microdroplets that will also be discussed later (Figure 8c).

The surface area of the bulk water was kept constant (133 mm^2) for all tested volumes. No influence of the water volume (i.e. the height of the water column in the bulk reactor) was detected for the same treatment time. This also shows that the total gas-water interface surface area is the key parameter determining the solvation.

Preprints (www.preprints.org) | NOT PEER-REVIEWED | Posted: 1 December 2020 doi:10.20944/preprints202012.0025.v1

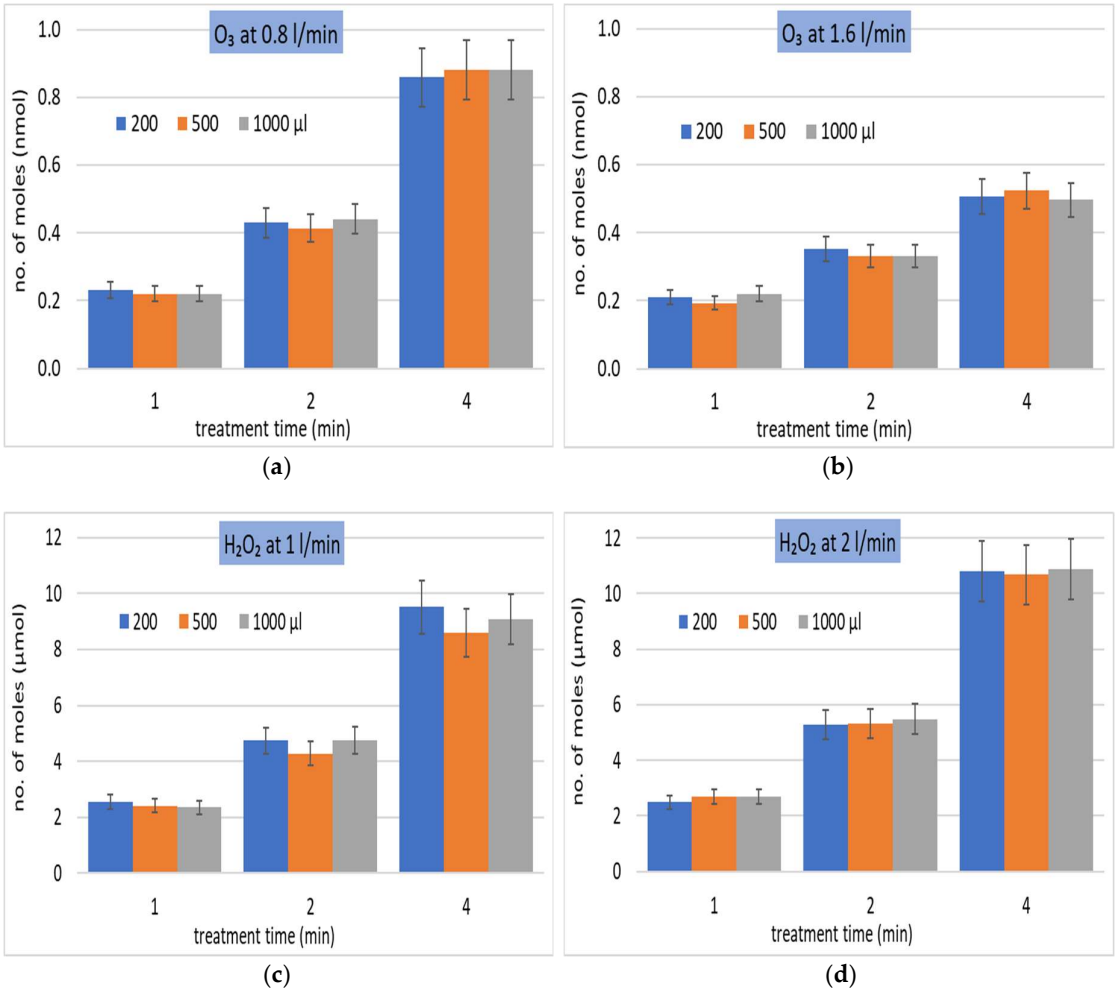

Figure 3. Solvation of O_3 and H_2O_2 at different gas flow rates (l/min) and water volumes (µl) during different treatment times (min) in bulk water. Total molar number of dissolved molecules as a function of treatment time, different water volumes, at constant gas-liquid interface area.

At the higher gas flow rate, the residence time of the gas inside the reactor, thus also gas-liquid interaction time, were shorter and the amount of dissolved O_3 decreased, despite the higher amount of O_3 delivered into the reactor per unit time (Figure 3a, b). On the other hand, for H_2O_2, the higher gas flow rate resulted in slightly higher solvation, due to the higher amount of H_2O_2 delivered into the reactor per unit time (Figure 3c, d), despite the shorter gas-liquid interaction time.

3.2. Solvation of O_3 and H_2O_2 in electrosprayed water droplets

When we apply a high voltage (V_a) on the needle nozzle through which the water is delivered to the reactor with a water flow rate (Q_w), the ES starts at 7.5 kV (at the lower Q_w) while the dc corona discharge plasma onset occurs at 9 kV. Figure 4 shows an example of electrosprayed microdroplets obtained by HS camera imaging. From a large set of HS camera images, we were able to estimate the size distribution of the ES water microdroplets (Figure 5). Besides V_a (Figure 5a), Q_w also influences this size distribution (Figure 5b). However, the differences do not seem to be very significant. In all histograms, the largest number of droplets have a diameter around 50 µm and there are only a few droplets with a diameter above ~ 150 µm. The abundance of these "big" droplets slightly decreases with increasing V_a and decreasing Q_w.

Preprints (www.preprints.org) | NOT PEER-REVIEWED | Posted: 1 December 2020 doi:10.20944/preprints202012.0025.v1

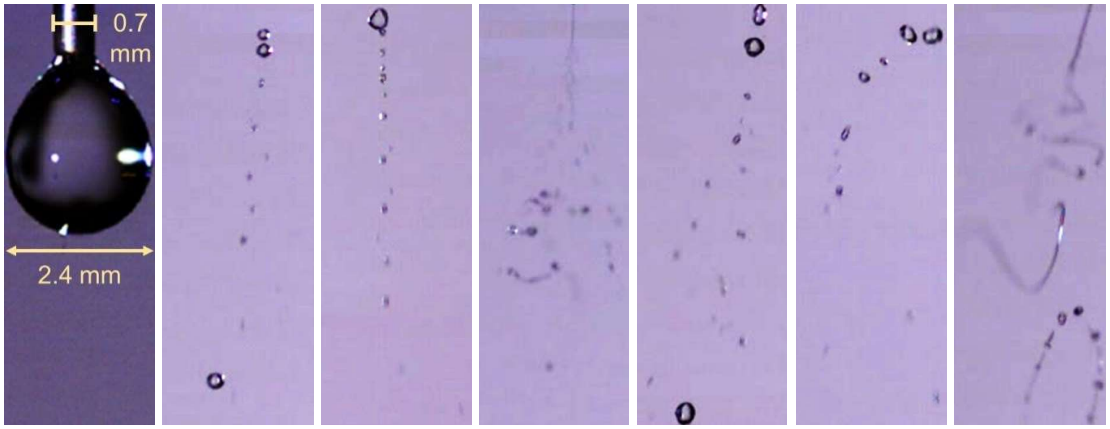

Figure 4. Examples of water droplets photographs by HS camera for different V_a (kV) and Q_w (µl/min): (**a**) 0 kV; (**b**) 9 kV, 300 µl/min; (**c**) 11 kV, 300 µl/min; (**d**) 13 kV, 300 µl/min; (**e**) 9 kV, 500 µl/min; (**f**) 11 kV, 500 µl/min; (**g**) 13 kV, 500 µl/min.

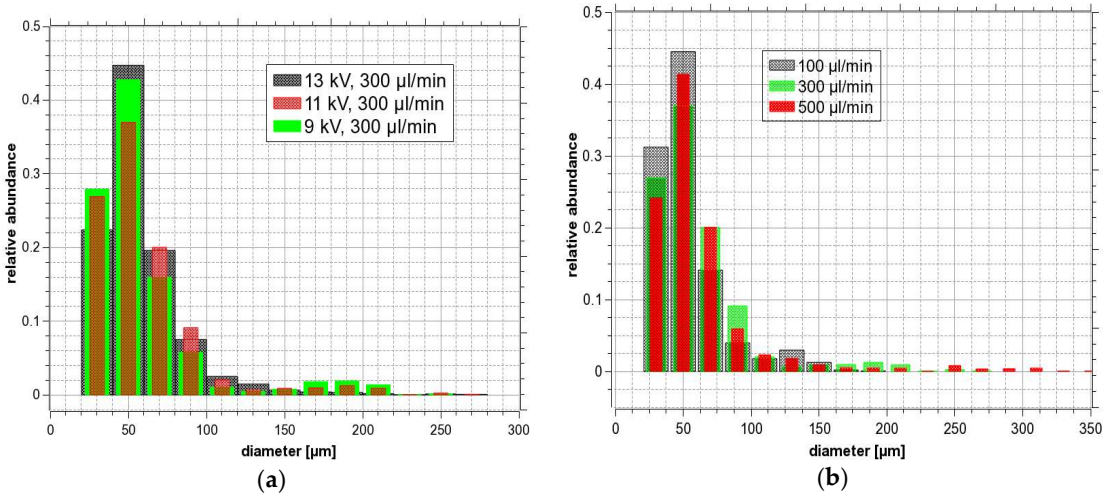

Figure 5. The relative abundance of water microdroplets produced by ES as a function of microdroplets diameter at different V_a (kV) and Q_w (µl/min): (**a**) 9, 11, 13 kV, and 300 µl/min; (**b**) 11 kV and 100, 300, 500 µl/min. Microdroplets with a diameter under 20 µm are below the detection limit of our camera imaging.

From the bulk water experiment, we know that the gas-liquid interface surface area is the key parameter determining the solvation. Therefore, we estimated the total surface area of the water ES droplets integrated for 1 minute, from the droplet size distributions. Figure 6 shows this total surface area for different Q_w as a function of V_a and it is compared with the surface area of the bulk water and water droplets (with diameter 1.5-2 mm) at 5 kV. There is a significant increase with increasing V_a and Q_w. At 13 kV and 500 µl/min for 1 minute, the produced total surface area is almost 190 times larger than the area during the bulk liquid experiment.

Preprints (www.preprints.org) | NOT PEER-REVIEWED | Posted: 1 December 2020 doi:10.20944/preprints202012.0025.v1

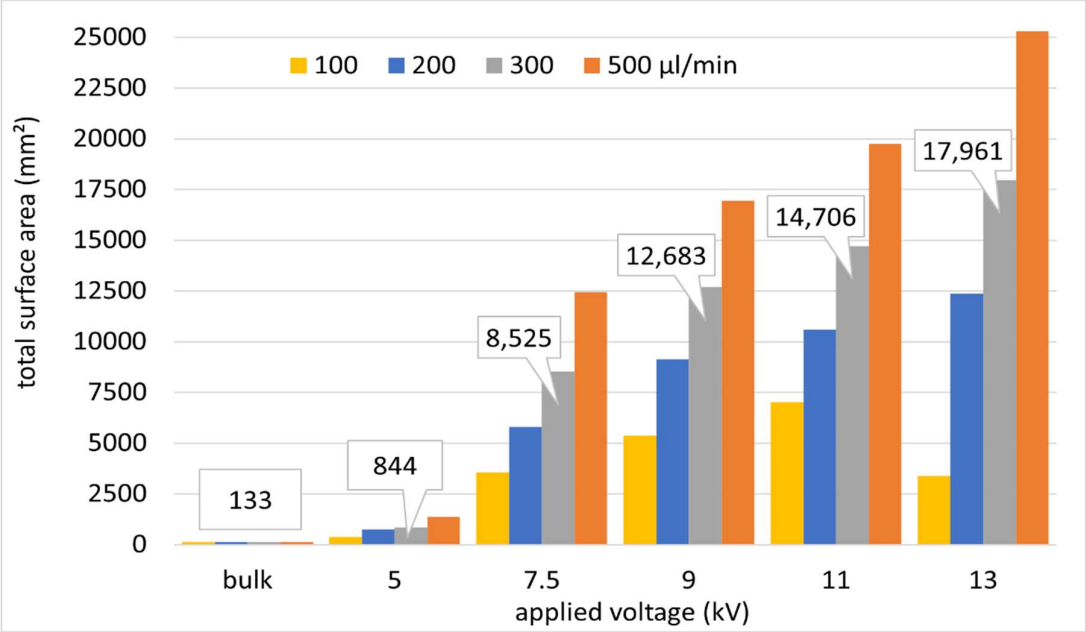

Figure 6. The total surface area of water droplets and microdroplets formed by ES during 1 minute for different Q_w (µl/min) as a function of V_a (kV), compared to the bulk water experiment.

In coherence with the bulk water experiment, the amount of dissolved O_3 and H_2O_2 into ES droplets increases with the treatment time, as shown in Figure 7a, b for O_3, and Figure 8b, c for H_2O_2. However, this solvation rate is slower than linearly proportional with time, as observed in the bulk water experiment. The dissolved O_3 and H_2O_2 also increase with increasing V_a and Q_w (Figure 7c, d for O_3 and Figure 8a, b for H_2O_2), although the effect of increasing Q_w is not so significant in some cases. These results prove more efficient solvation of O_3 and H_2O_2 into ES microdroplets compared to the bulk liquid, but they also show that the observed effect cannot be explained simply by the measured droplet size distribution and their total surface area. The real limitation in the ES experiment is the limited lifetime of the generated flying water microdroplets.

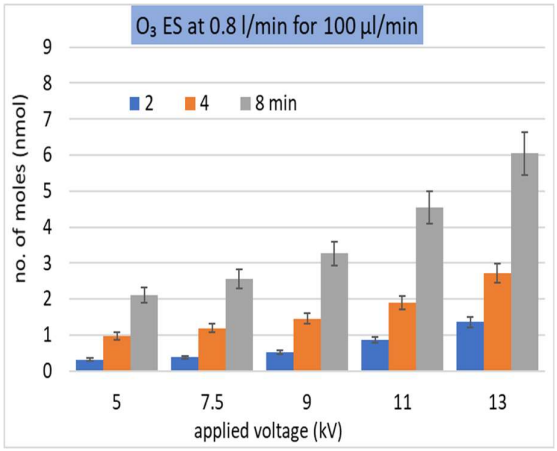

(a)

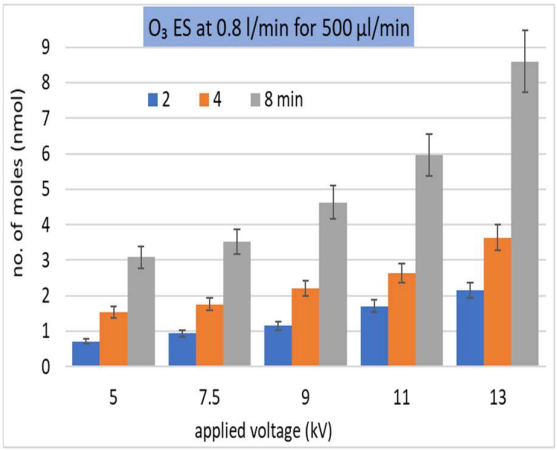

(b)

Preprints (www.preprints.org) | NOT PEER-REVIEWED | Posted: 1 December 2020 doi:10.20944/preprints202012.0025.v1

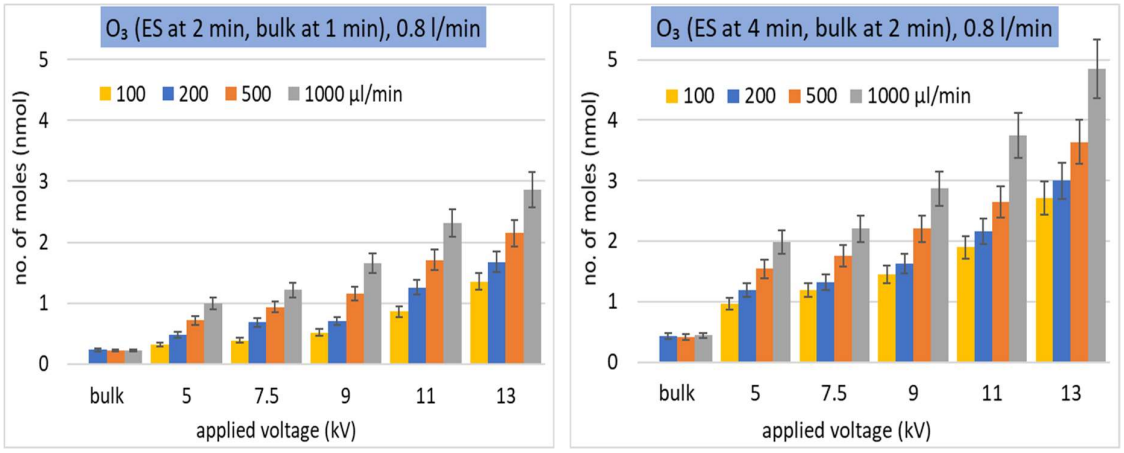

(**c**) (**d**)

Figure 7. Solvation of O_3 as a molar number of dissolved molecules in ES at a constant gas flow rate (l/min). (**a**), (**b**) two values of constant Q_w (µl/min) and different treatment times (min); (**c**), (**d**) different Q_w (µl/min) during different treatment times (min) in ES and bulk water.

We must note that the decrease of O_3 concentration in the gas phase was not measurable at the resolution of 0.3 ppm of our O_3 gas sensor. On the other hand, we observed a measurable depletion of H_2O_2 in the gas phase, both in the bulk and ES experiments. The amount of remaining H_2O_2 in the gas phase limits the concentration achievable in the liquid phase (this issue will be discussed later in detail). Measured concentrations (number of moles) of dissolved H_2O_2 fits well with the molar amount of H_2O_2 depleted from the gas phase (Figure 8c, d) within the experimental uncertainty.

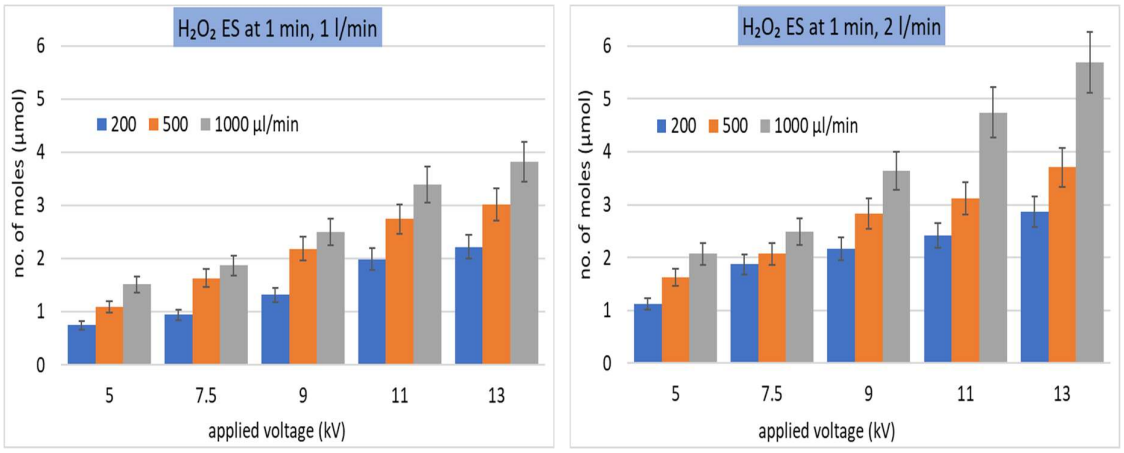

(**a**) (**b**)

Preprints (www.preprints.org) | NOT PEER-REVIEWED | Posted: 1 December 2020 doi:10.20944/preprints202012.0025.v1

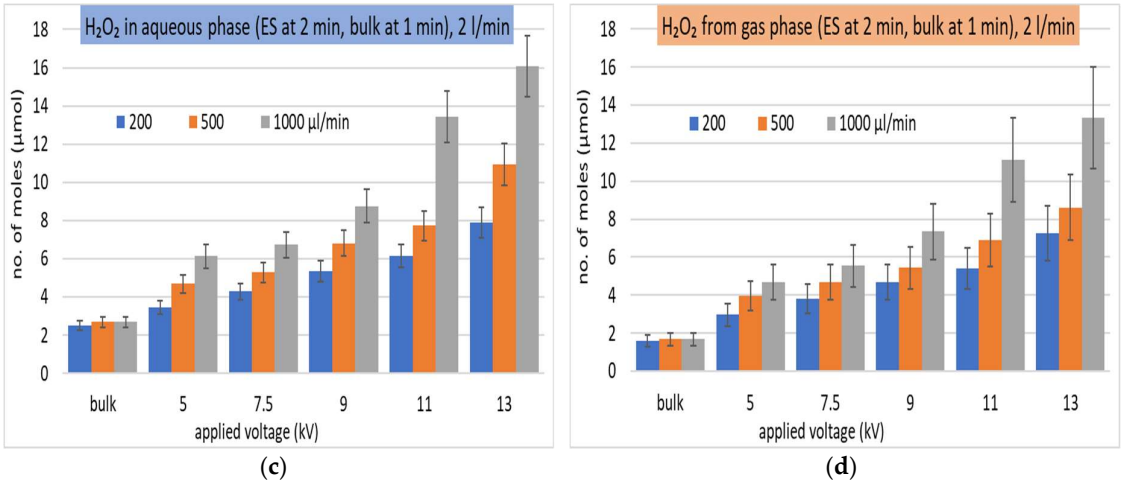

Figure 8. Solvation of H_2O_2 as the molar number of dissolved molecules in ES. (**a**), (**b**) different gas flow rates (l/min) and Q_w (µl/min) during 1 min treatment time; (**b**), (**c**) the same gas flow rate 2 l/min and different treatment times (min) in ES and in (**c**) also bulk water added; (**d**) depleted H_2O_2 from the gas at the conditions of (**c**).

Let us go back to the limited lifetime of the electrosprayed microdroplets. During the ES process, the microdroplets fly from the needle nozzle towards the bottom of the reactor. The relevant lifetime of the microdroplets is not the duration of the experiment, but the time between their formation and the moment when they hit the bottom of the reactor. The lifetime of these microdroplets can be calculated from their traveled path and their speed v_d. Figure 9 shows the distribution of their speed as a function of their diameter, as measured by the HS camera. The shortest possible path of a droplet which moves perpendicularly to the ground is 2.5 cm, but the real path of a droplet deviated from the axis of the reactor can be as long as ~ 3 cm. For the biggest and the slowest microdroplets (v_d ~ 3.5 m/s), we thus get the longest lifetime up to ~ 9 ms.

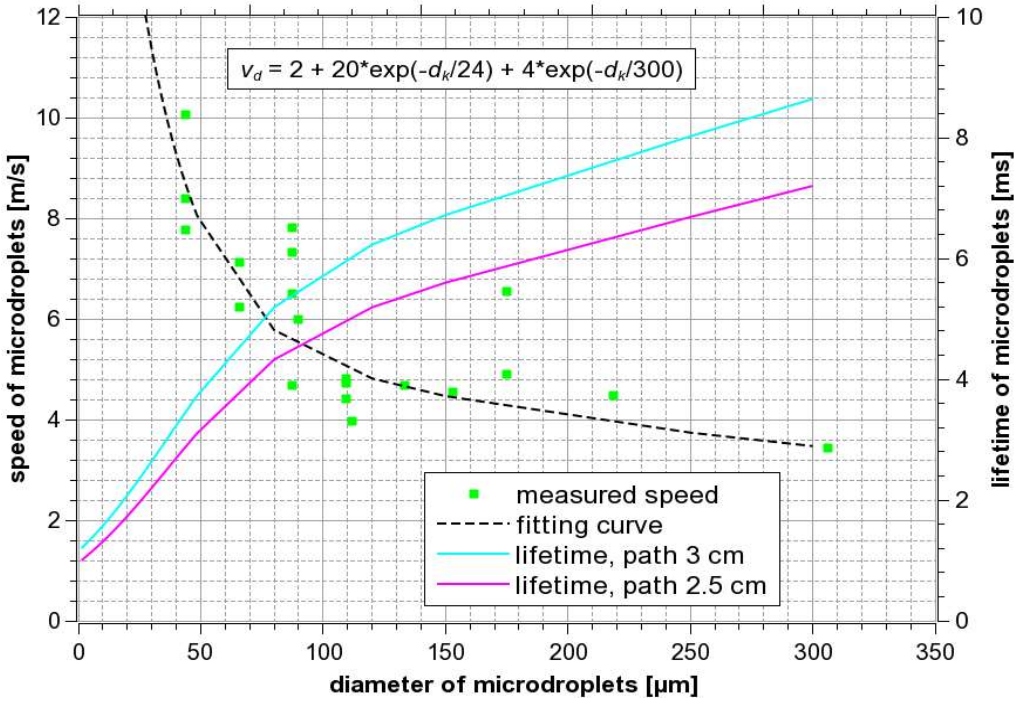

Figure 9. Speed of ES microdroplets measured from the HS camera images and their lifetime as a function of their diameter d_k.

Preprints (www.preprints.org) | NOT PEER-REVIEWED | Posted: 1 December 2020 doi:10.20944/preprints202012.0025.v1

Compared to the interaction (i.e. treatment) time during the bulk experiment (1-4 min, i.e. order of 100 s), the lifetime of flying microdroplets is by 4-5 orders of magnitude shorter. Taking into account that the total surface area of ES microdroplets is augmented much less with respect to their much shorter lifetime compared to the bulk (the highest measured total surface area augmentation factor was 190 at 13 kV and 500 μl/min), we should in fact observe a lower amount of dissolved O_3 and H_2O_2 into ES droplets compared to the bulk water. This contradicts the experimental results. To resolve this problem, it is necessary to consider the effect of microdroplets which stay as separated microdroplets for a certain time even after they hit the bottom of the reactor. They could stay at the bottom like these separated droplets for a much longer time than just a few ms before they merge to form bigger droplets and eventually a uniform bulk liquid.

In the real ES experiment with a constant Q_w running for a specific treatment time, the total amount of dissolved O_3 and H_2O_2 molecules is given by the sum of those dissolved during the short lifetime of flying microdroplets, then the molecules absorbed by microdroplets sitting at the bottom of the reactor, and finally by merged bigger droplets (eventually forming bulk liquid) formed later during the experiment. There are also some sprayed microdroplets sitting on the walls of the ES reactor due to the ES process. The amount of these sprayed droplets is increased with the increase of Q_w, V_a, and the treatment time. Contribution of various phases (flying, bottom, and sprayed droplets, besides the formed bulk) to H_2O_2 and O_3 solvation into the liquid water will be discussed in the next section, based on a comparison of theoretical calculations with the experimental results.

4. Discussion

4.1. Theory of mass transfer from gas to the liquid phase. The role of surface area

In the first approximation let us assume that all the solvation process is guided by the surface area with the equilibrated transfer of molecules of the same species i from the gas into the liquid phase and the backward transfer of molecules from the liquid into the gas phase.

First, let us express the flux of molecules from the gas into the liquid phase:

$$j_i^+ = \frac{1}{4} n_i \overline{v_i} = \frac{\overline{v_i}}{4k_B T} p_i = \beta p_i, \quad (3)$$

Here, n_i is the density of i-th species, v_i is the mean chaotic velocity of these molecules, k_B is the Boltzmann constant, T is the gas temperature, and p_i is the partial pressure of i-th molecules.

Next, we can assume that the flux of i-th species from the liquid phase back to the gas phase is proportional to its molar concentration in the liquid phase c_i:

$$j_i^- = \alpha c_i, \quad (4)$$

In the steady state, these two fluxes are equal. It is possible to derive the constant α using Henry's law coefficient k_H^i, because in the steady state:

$$c_i = \frac{\beta}{\alpha} p_i = k_H^i p_i, \quad (5)$$

Knowing the fluxes in both directions, the number of transferred molecules ΔN_i in time Δt_i into the liquid phase with surface area S can be expressed as

$$\Delta N_i = (\beta p_i - \alpha c_i) S \Delta t, \quad (6)$$

In combination with the expression $c_i = N_i/(N_A V)$, where V is the volume of the liquid phase and N_A is the Avogadro constant, we can derive an equation describing the evolution of c_i:

$$\frac{dc_i}{dt} = \frac{S\beta p_i}{N_A V} - \frac{S\beta}{N_A V k_H^i} c_i, \quad (7)$$

Assuming an initial concentration in the liquid phase to be zero, $c_i(0) = 0$, we obtain this expression for the aqueous concentration of the i-th species at time t:

Preprints (www.preprints.org) | NOT PEER-REVIEWED | Posted: 1 December 2020 doi:10.20944/preprints202012.0025.v1

$$c_i(t) = p_i k_H^i \left(1 - exp\left(\frac{-S\beta}{N_A V k_H^i} t\right)\right), \quad (8)$$

In this simplified theory, we assumed that the partial pressure of species i did not change in time and that the concentration in the liquid phase was homogeneous. This equation is valid both for bulk liquid as well as for microdroplets. If we consider only spherical droplets with diameter d_k, we finally get an expression where m_i is the mass of i-th molecules.

$$c_i(t) = p_i k_H^i \left(1 - exp\left(\frac{-6t}{N_A d_k k_H^i \sqrt{2\pi m_i k_B T}}\right)\right), \quad (9)$$

We can see that $c_i(t)$ converges towards a saturated concentration $c_i^{satur.}$ with the increasing time. To be able to compare results for O_3 and H_2O_2, it is better to look at the evolution of the **saturation degree** ξ_i defined as $\xi_i(t) = c_i(t)/c_i^{satur.}$. Figure 10 depicts examples of the saturation degree time evolutions calculated by this simple theory based on fluxes inside and outside of droplets.

The saturation will be reached relatively slowly in the case of H_2O_2 (Equation 9, Figure 10) due to the large Henry's law coefficient. Let us apply this theory to the solvation of H_2O_2 in bulk water. We must consider how many molecules are needed to achieve saturation in the liquid. With the gaseous concentration of H_2O_2 ~ 100 ppm (~ 2.46×10^{15} cm^{-3}), the saturated concentration in liquid water is ~ 10 M. Thus, approximately 6×10^{21} molecules must be dissolved to achieve the saturation and more than 2×10^3 liters of the gas passing through the reactor would be needed. With the gas flow of 1 l/min at input concentration 100 ppm, even if we assumed that all H_2O_2 is dissolved and nothing leaves out from the reactor, such an experiment would take more than 33 hours. This figure would be even larger because not all gaseous H_2O_2 molecules can be dissolved.

The average residence time of the gas in the bulk reactor with ~ 1.4 cm^3 volume, the depth of the bulk liquid H, and the gas flow rate 1 l/min, is approximately 0.08 s. If we estimate the dissolved amount of H_2O_2 into the bulk water using the theoretical Equation (8), we find out that for H = 7.54 mm (1000 μl of water in the reactor) and time 0.08 s, only about 37% of available H_2O_2 molecules can dissolve. At H = 3.77 mm (500 μl) and H = 1.51 mm (200 μl), 60% and 89% of the H_2O_2 can be dissolved within 0.08 s, respectively.

Taking all this into account, we estimated the expected saturation degree for H_2O_2 as a function of time and H and compared it with experimental results (Figure 11). We observe quite a good agreement between the theoretically calculated and the experimental saturation degrees, except for H = 1.51 mm. Here, significantly less H_2O_2 can be dissolved within the gas residence time inside the reactor than predicted. This could be explained by the fact that at H = 1.51 mm, the depletion of H_2O_2 from the gas is already too high and the saturation concentration of H_2O_2 in the liquid phase should be lower than the expected maximum 10 M, corresponding to the lower concentration of H_2O_2 in the gas phase.

The H_2O_2 depletion from the inlet air and so its insufficient amount in the vicinity of the gas-water interface can also explain why only ~ 10^4 times more H_2O_2 than O_3 was solvated, although Henry's law coefficient of H_2O_2 is larger by 7 orders of magnitude than that of O_3.

Preprints (www.preprints.org) | NOT PEER-REVIEWED | Posted: 1 December 2020 doi:10.20944/preprints202012.0025.v1

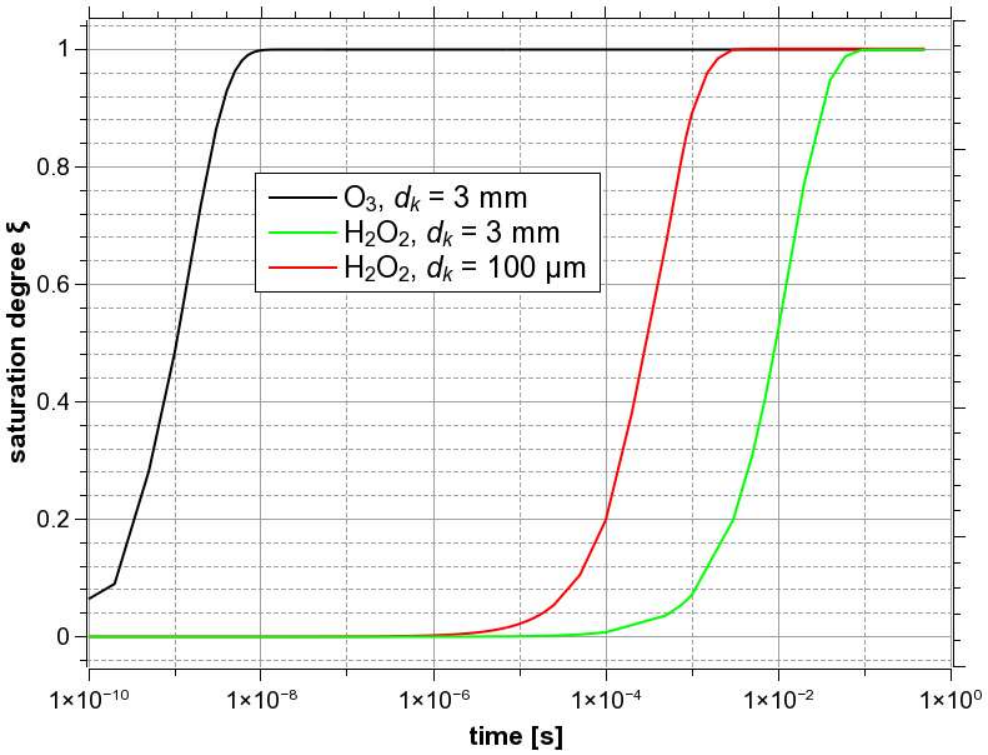

Figure 10. Examples of saturation degree time evolutions calculated by a simple theory (Equation 9) based on fluxes inside and outside of droplets.

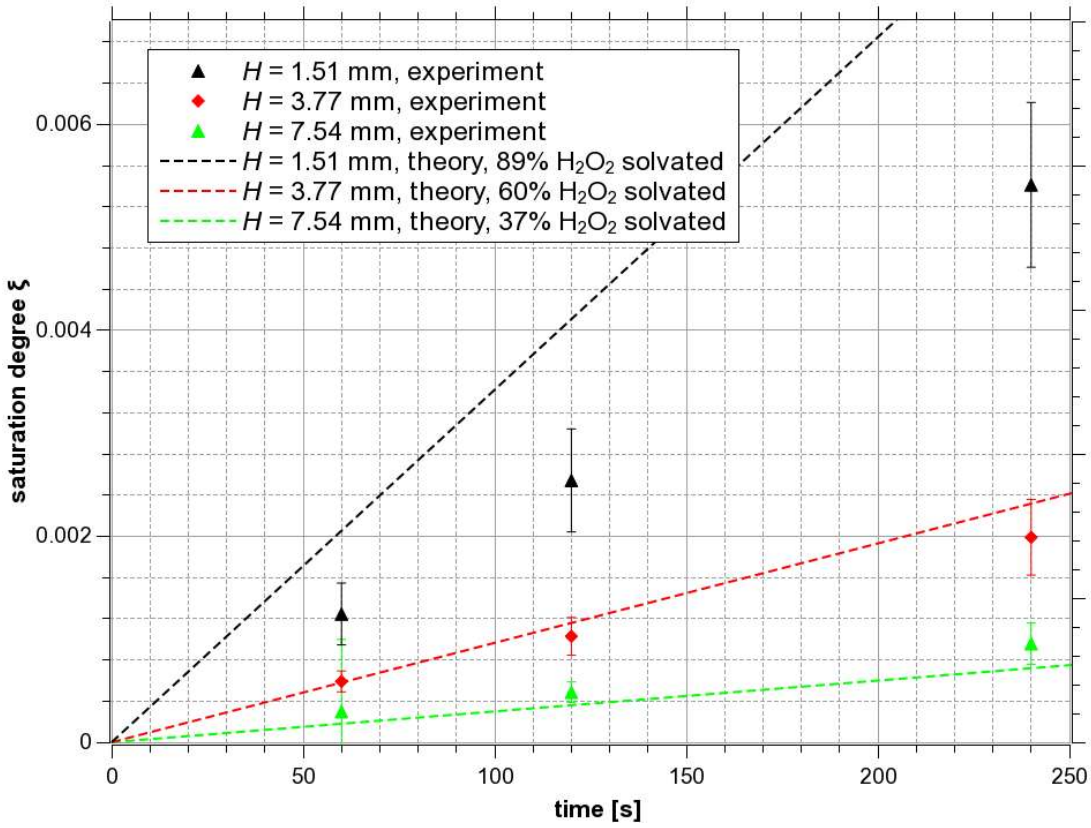

Figure 11. Saturation degree ξ_{H2O2} of H_2O_2 as a function of treatment time and bulk water depth H.

Preprints (www.preprints.org) | NOT PEER-REVIEWED | Posted: 1 December 2020 doi:10.20944/preprints202012.0025.v1

The real situation is even more complicated for ozone and this simple solvation theory is not sufficient. For O_3, with a very low Henry's law coefficient, the formula (9) predicts very fast saturation of water by dissolved ozone even for large droplets with d_k = 3 mm (Figure 10), as well as for the bulk liquid. This means that even without the ES, the droplets with a diameter of 3 mm would be saturated by O_3 almost immediately at the moment when they are created, long before they hit the reactor bottom. The bulk liquid water would also be saturated in less than one second. This contradicts our experimental findings (Figures 3 and 7) that the gas-liquid interaction time determines the solvation.

The major problem of the above theoretical considerations is the assumption that the dissolved molecules spread immediately inside the entire droplet. To correct this theory, we must take into account the fact that the dissolved species concentration inside the liquid equalizes only very slowly by diffusion. It is only a thin layer next to the surface that becomes saturated quickly.

Thus, we must take into account the diffusion of dissolved molecules inside the liquid water that will make the characteristic saturation time longer.

4.2. O_3 diffusion into the bulk liquid

In a 1-dimensional situation (bulk liquid) we can estimate the distance L to which O_3 will diffuse during a given time by a simple equation

$$L \sim \sqrt{2D_{O3}t}, \tag{10}$$

where D_{O3} is the diffusion coefficient of O_3 in water. At 300 K, D_{O3} = 2 × 10^{-5} cm^2/s [62]. To simplify the calculation, we can assume that the surface area is quickly saturated by dissolved O_3 molecules and their concentration there can be considered as constant ($c_{O3}^{satur.}$). We can use the 1-dimensional theory of diffusion to describe the concentration evolution in time and depth h of the bulk liquid.

$$c_{O3}(h,T) = c_{O3}^{satur.} exp\left(\frac{-h^2}{4D_{O3}t}\right), \tag{11}$$

Integration from 0 to H (the total depth of the bulk liquid) gives us the average concentration in a given time and hence the degree of saturation ξ_{O3} as a function of time and H (Equation 12)

$$\xi_{O3}(H,t) = \frac{\int_0^H exp\left(\frac{-h^2}{4D_{O3}t}\right)dx}{H}, \tag{12}$$

Figure 12 shows the calculated saturation degree time evolutions for three different values of H: 1.51 mm, 3.77 mm, and 7.54 mm (they correspond to the water volumes 200 µl, 500 µl, and 1000 µl in the bulk reactor, respectively). With H = 3.77 mm and the treatment time 4 min (240 s), the theoretical average concentration of O_3 should reach only about 32 % of the saturation level. For H = 7.54 mm, this number is even lower (16 %). The theoretical curves are compared with experimental results in Figure 12. There is a relatively good agreement within the experimental uncertainty, except for H = 1.51 mm, where experimental values are below the theoretical ones. At H = 1.51 mm the amount of water is very small (200 µm). Even slight vibrations and shivering of the water surface due to the gas flow can have a significant influence on the O_3 solvation inside the bulk liquid.

Preprints (www.preprints.org) | NOT PEER-REVIEWED | Posted: 1 December 2020 doi:10.20944/preprints202012.0025.v1

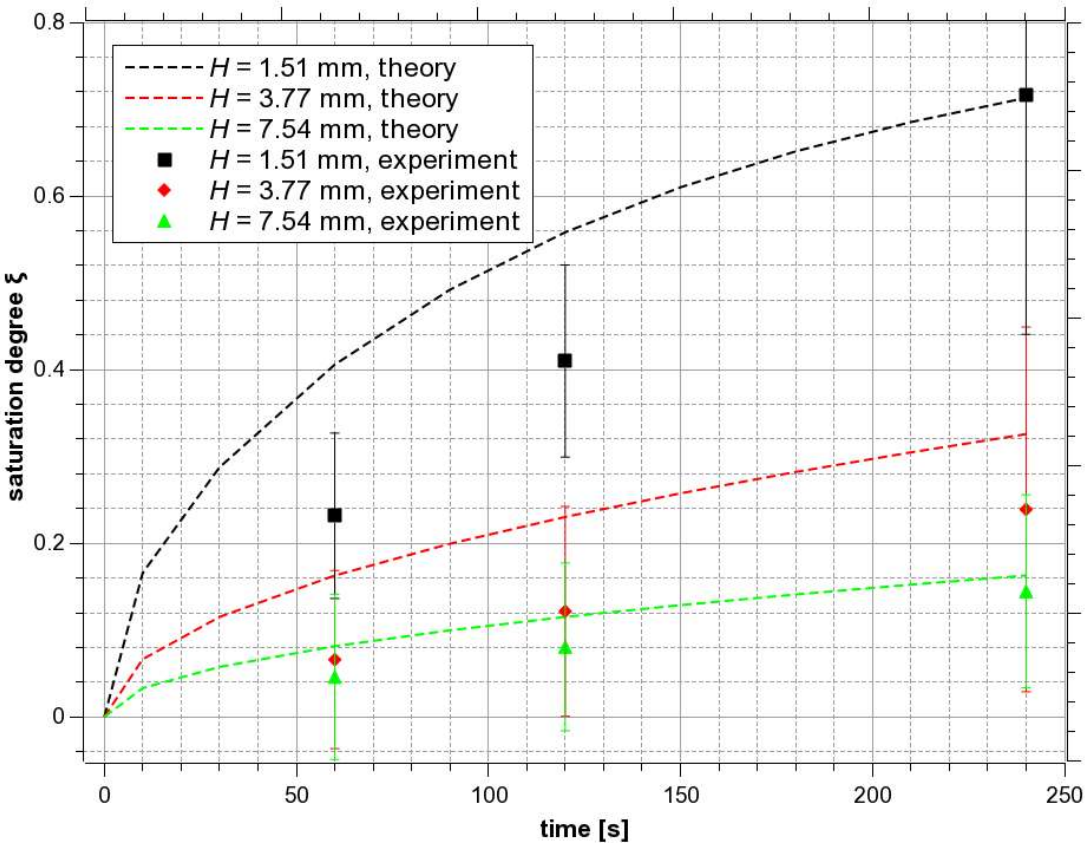

Figure 12. Saturation degree ξ_{O3} of O_3 as a function of treatment time and bulk water depth *H*.

4.3. O_3 diffusion in microdroplets

Like in the bulk liquid, the calculation is easier if we assume that the surface area is quickly saturated by O_3 molecules and the concentration here can be considered as constant ($c_{O3}^{satur.}$). Next, we estimate the saturation degree ξ_{O3} in the droplets as a function of time and r_k (droplet radius). We approximate the concentration of dissolved O_3 inside the droplet as a function of time and radial coordinate *r* by the function

$$c_{O3}(r,t) = c_{O3}^{satur.} exp\left(\frac{-(r_k-r)^2}{4D_{O3}t}\right), \quad (13)$$

The saturation degree by ozone ξ_{O3} as a function of time and r_k in spherical coordinates can be then calculated by Equation (14)

$$\xi_i(r,t) = \frac{3\times\int_0^{r_k} r^2 exp\left(\frac{-(r_k-r)^2}{4D_i t}\right)dr}{r_k^3}, \quad (14)$$

As we already mentioned, the longest expected lifetime of generated microdroplets is ~ 10 ms. Therefore Figure 13 shows the estimated saturation degree for droplets with different diameters in the time scale up to 10 ms.

Preprints (www.preprints.org) | NOT PEER-REVIEWED | Posted: 1 December 2020 doi:10.20944/preprints202012.0025.v1

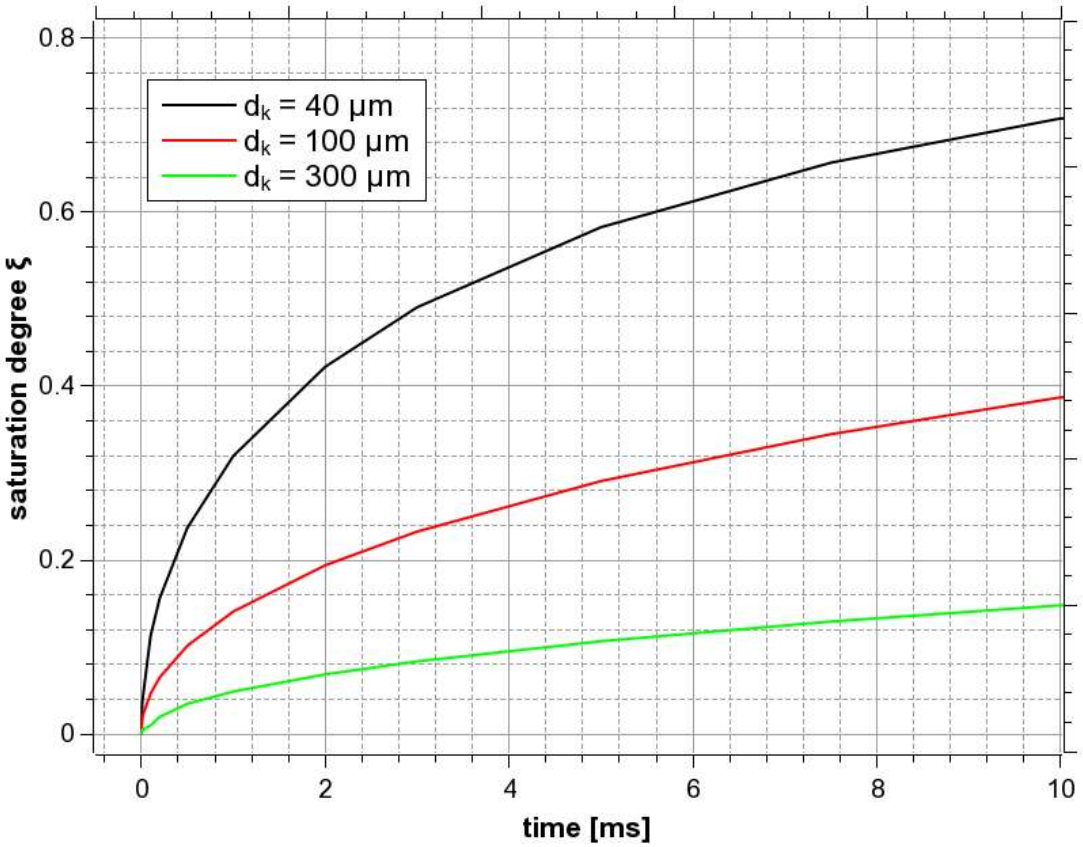

Figure 13. Estimated evolution of saturation degree ξ_{O3} of O_3 as a function of time and diameter of flying microdroplets, calculated for O_3 diffusion in the water microdroplets at 300 K.

From Figure 13 we can conclude that only very small microdroplets with a diameter below ~ 40 µm could be saturated within this time of ~10 ms scale. To achieve the highest solvation rate, it would be thus preferable if all droplets had this diameter (or lower). Our measurements show that most of the detected droplets have a slightly larger diameter, around 50 µm (Figure 5). In real ES, the average size of the microdroplets might be even smaller, because we were not able to detect droplets with a diameter below ~ 20 µm by our imaging technique with the resolution of 21.875 µm /pixel.

However, the droplet size distribution histograms shown in Figure 5 do not reflect that the overall saturation degree depends significantly on the volume of droplets. If we merge 10 tiny ozone-saturated droplets (d_k = 10 µm) with 1 larger droplet with d_k = 200 µm and ξ_{O3} = 0.1, the resulting ξ_{O3} would be only 0.100125. For this reason, we recalculated the data from Figure 5a to show the relative contribution of droplets with different diameters to the total volume $P^v(d_k)$. In this representation (Figure 14), the contribution of the tiny droplets is minimal. For verification, we artificially modified the size distribution histogram measured at 13 kV and 300 µl/min. We doubled the number of droplets with a diameter of 20-40 µm and we added droplets with a diameter below 20 µm as if their relative abundance were ~ 37 %. The influence of this modification on $P^v(d_k)$ was almost negligible (Figure 14). We can see that there is a significant difference between $P^v(d_k)$ at 9 and 13 kV, although the difference between 9 and 13 kV seemed to be negligible in the original size distribution histogram of the droplets (Figure 5a).

Preprints (www.preprints.org) | NOT PEER-REVIEWED | Posted: 1 December 2020 doi:10.20944/preprints202012.0025.v1

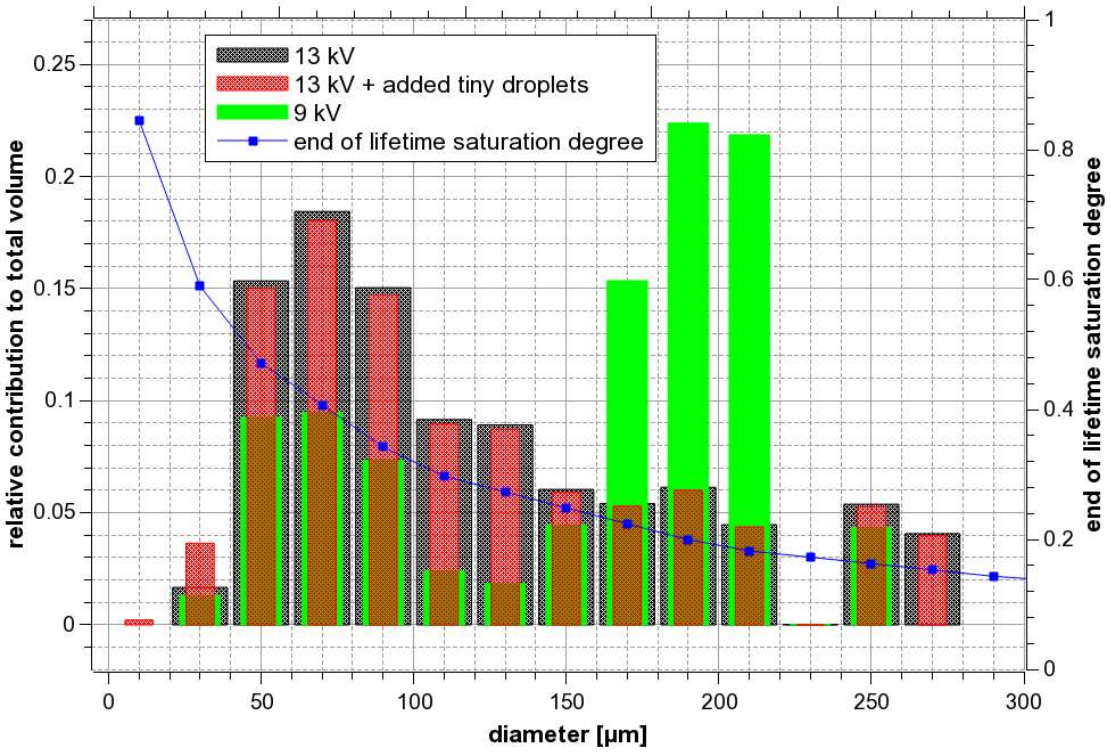

Figure 14. Relative contribution of the droplets with different diameters to the total volume $P^v(d_k)$ and saturation degree at the end of their lifetime $\xi^{fin}(d_k)$ as a function of droplet diameter, V_a = 9 and 13 kV, Q_w = 300 µl/min.

Figure 14 also shows $\xi^{fin}(d_k)$, the saturation degree of O_3 at the end of the droplet lifetime (Figure 9, path 3 cm) as a function of droplets diameter. Finally, we can define the effective saturation degree ξ^{eff} of droplets hitting the bottom of the reactor by integrating the product of $P^v(d_k)$ with $\xi^{fin}(d_k)$ over the entire range of diameters:

$$\xi^{eff} = \int_{d_k} \xi^{fin}(d_k) P^v(d_k) \mathrm{d}d_k, \quad (15)$$

Figure 15 shows the ξ^{eff} calculated for all V_a and Q_w, which increases with the applied voltage that shifts the relative contribution distribution towards the smaller diameter droplets (Fig. 14) As we can see there is no significant dependence on the Q_w, though ξ^{eff} is probably slightly smaller at 500 µl/min than at lower Q_w. This could mean slightly bigger droplets on average. On the other hand, ξ^{eff} calculated at 100 µl/min is probably slightly higher than at higher Q_w, except for V_a = 13 kV, when the formation of microdroplets was most probably influenced by the onset of corona discharge. The increase of ξ^{eff} with increasing V_a can partly explain the increase of the dissolved O_3 amount with increasing V_a (Figure 6). For a more precise explanation of the observed dependence of solvation on V_a, we must also consider the microdroplets sitting at the bottom.

Preprints (www.preprints.org) | NOT PEER-REVIEWED | Posted: 1 December 2020 doi:10.20944/preprints202012.0025.v1

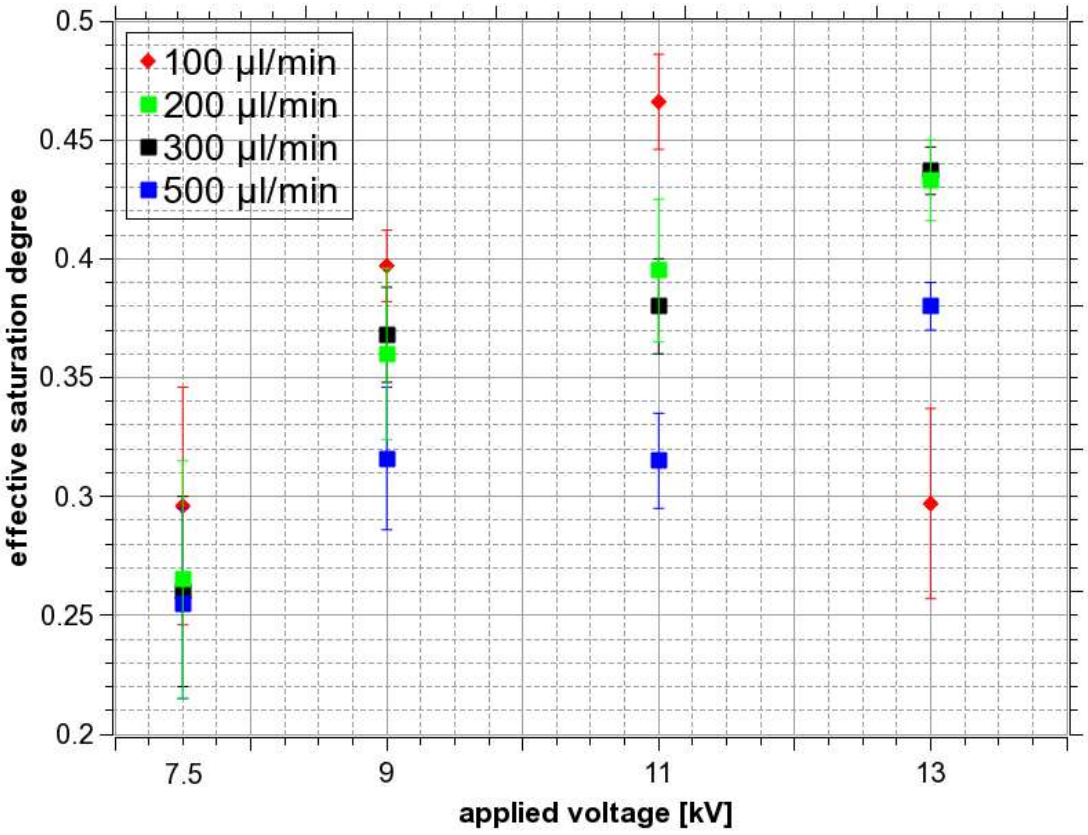

Figure 15. Effective O_3 saturation degree ξ^{eff} of flying microdroplets as a function of V_a (kV) at different Q_w (µl/min).

To estimate the role of microdroplets sitting at the bottom of the reactor, we have to consider some simplifications. We will further assume that these bottom microdroplets are semi-spheres (with a contact angle 90º) with the same volume as their parent microdroplets from the ES. Consequently, their diameter d_s will be slightly bigger than the diameter of their parent microdroplets (d_s ~ 1.26 d_k). Next, we can estimate the saturation degree reached in these bottom microdroplets if we know their lifetime (τ_s). Water flow rate Q_w is constant during the experiment and if they do not coagulate, their average lifetime would be equal to ½ of the total treatment time. Thus, for the Q_w of 200 µl/min, the total water volume 1 ml would be collected at the bottom in 5 minutes (300 s) and the average lifetime of bottom microdroplets would be 150 s. In reality, this average lifetime of bottom microdroplets is certainly lower, as we explain in the following section.

In the ES experiment, the droplets are sprayed into a relatively wide solid angle. As a result, they are distributed all over the reactor bottom (even walls) in the initial phase. Gradually, bigger droplets start to be formed at places with the highest flux of merging droplets. This process decreases the average lifetime of bottom microdroplets. Moreover, as the reactor bottom gets gradually more and more covered by big droplets, more and more incoming microdroplets hit these big droplets instead of the clean surface of the reactor bottom, having thus the bottom lifetime τ_s = 0 s. A correct assessment of the bottom droplets' lifetime will require further studies. Here, as for the first approximation, we can estimate the saturation degree of the bottom microdroplets using τ_s = 1-10 s as shown in Figure 16. As we can see from Figure 16, for d_s = 300 µm (corresponding to the parent microdroplets with d_k = 238 µm), the saturation degree will exceed 90% within τ_s = 10 s, even starting from the saturation degree 0. This shows that the solvation into bottom microdroplets plays a significant role in our experiment, even if their average lifetime is in the order of 1 s, which is still much longer than the lifetime of flying microdroplets (~10 ms).

Preprints (www.preprints.org) | NOT PEER-REVIEWED | Posted: 1 December 2020 doi:10.20944/preprints202012.0025.v1

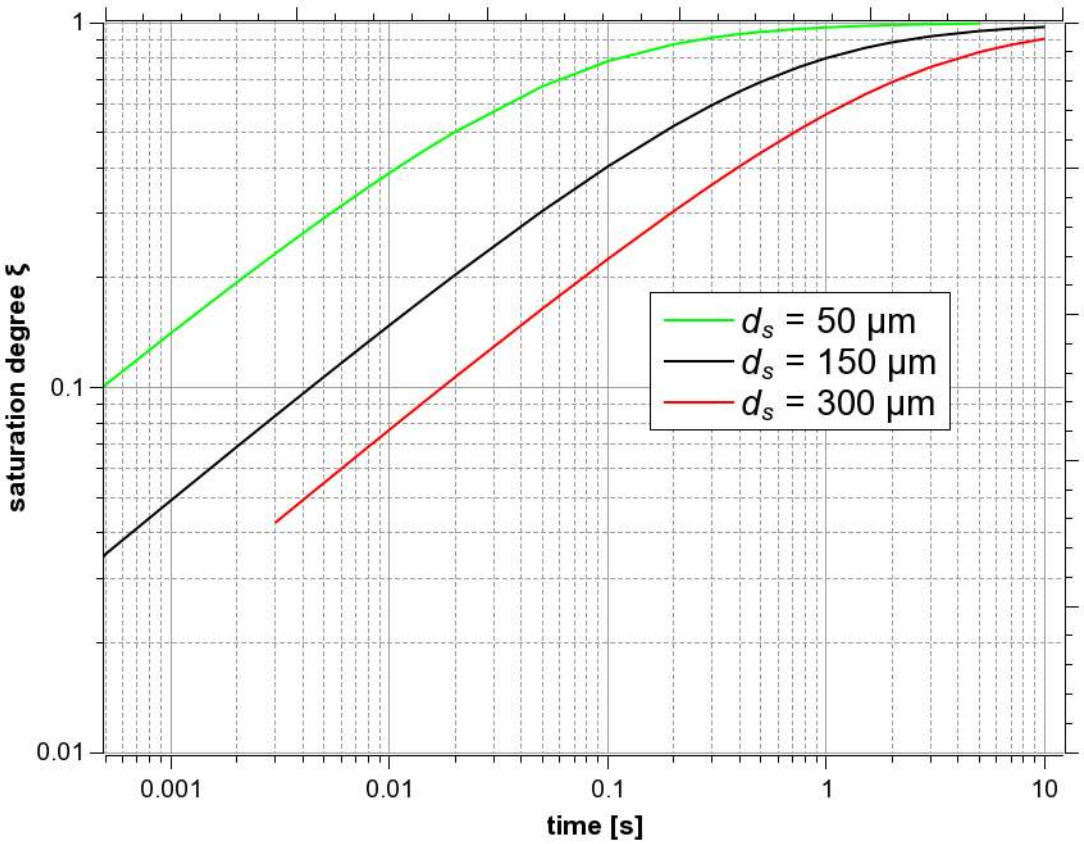

Figure 16. Estimated evolution of saturation degree ξ_{O3} as a function of time and diameter of bottom microdroplets, calculated for O_3 diffusion in the water at 300 K, time span up to 10 s.

4.4. Roles of flying microdroplets, sitting bottom microdroplets vs. solvation in the formed bulk

The calculated effective saturation degree ξ^{eff} of flying microdroplets (Figure 15) can help us to assess the importance of flying microdroplets vs. sitting bottom microdroplets vs. formed bulk water solvation of O_3. We have to compare ξ^{eff} to the measured ξ_{O3} values under various experimental conditions. It is demonstrated in Figure 17.

First, let us look at the ES experiment with Q_w of 500 µl/min and a treatment time of 2 min. The total amount of collected water is 1000 µl. Q_w is relatively high, and the bulk liquid is quickly formed and then exists during most of the treatment time. The contribution of bottom microdroplets should be thus small. We can estimate the contribution of the solvation in the formed bulk from the experiment with bulk water with volume 1000 µl (H = 7.54 mm) and the duration 1 min (1/2 of the ES experiment time, because in the ES experiment the average water residence time inside the reactor is ½ of the treatment time), where we achieved the saturation degree only around 0.045 (violet dashed line at the bottom of Figure 17). Thus, in the ES experiment even at low V_a = 7.5 kV, where ξ_{O3} is significantly higher (~ 0.25) than the bulk (0.045), the saturation must be mostly achieved thanks to the flying microdroplets. This can explain a good correlation between the measured ξ_{O3} and ξ^{eff} for Q_w = 500 µl/min in Figure 17.

Second, let us consider the ES experiment with the Q_w only 100 µl/min, with no formed bulk and no big droplets formation during most of the treatment time. Thus, the contribution of bottom droplets should be crucial, while the contribution of the O_3 solvation into the formed bulk should be small, although, in the bulk water experiment with the volume 200 µl (H = 1.51 mm) and duration 1 min, we achieved the saturation degree $\xi_{O3} \approx 0.23$. In the ES experiment, even at low V_a 7.5 kV, ξ_{O3} reached almost 0.4. The formed bulk solvation contribution would be even less important at higher V_a, where the advantage of flying and bottom microdroplets is already clearly

Preprints (www.preprints.org) | NOT PEER-REVIEWED | Posted: 1 December 2020 doi:10.20944/preprints202012.0025.v1

visible because ξ_{O3} grows with increasing V_a up to 1.12 ± 0.57. When comparing the ES experiment with Q_w 500 µl/min and 100 µl/min, we can see that the significant increase of ξ_{O3} should be mostly due to the sitting bottom droplets. This also explains a high experimental uncertainty of the measured ξ_{O3}. The coagulation of microdroplets and big droplet formation is significantly different in each individual experiment.

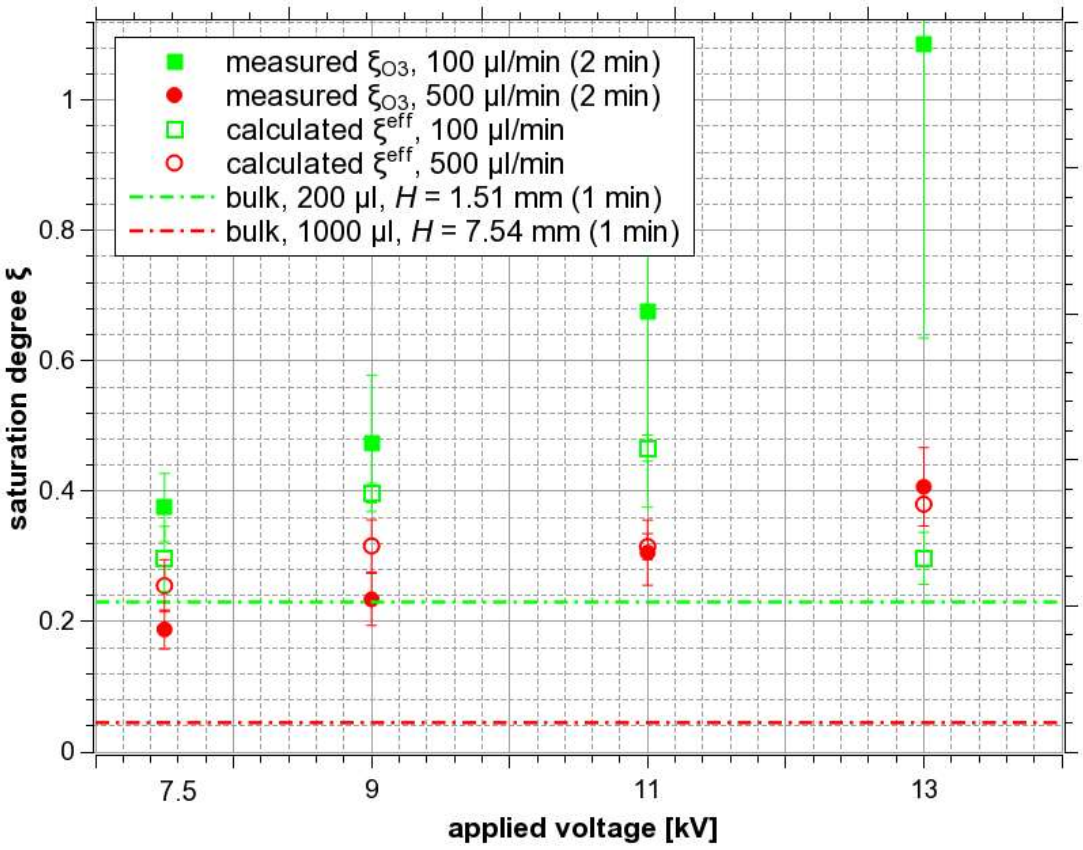

Figure 17. Comparison of O_3 ξ^{eff} calculated from the size distribution histograms (Figure 5) of flying microdroplets with the measured ξ_{O3} of bottom microdroplets two sets of ES experiments (Q_w = 100 and 500 µl/min), and O_3 saturation in the corresponding bulk experiments.

Parallel to O_3, we can also assess the role of flying and bottom microdroplets from the results of H_2O_2 solvation in the ES experiments. The situation is slightly different than in the case of O_3 and we cannot use the effective saturation degree ξ^{eff}, since it was calculated by considering O_3 diffusion, assuming instantaneous saturation of a thin surface layer. As we discussed earlier, there are not enough H_2O_2 molecules in the gas during the experiments to achieve saturation in water and the gaseous concentration of H_2O_2 is significantly depleted. Contribution of various phenomena (flying droplets, bottom droplets, formed bulk) to H_2O_2 absorption into liquid water should rather be demonstrated on the **solvation efficiency** parameter η_{H2O2}, which determines how many of the total H_2O_2 molecules from the gas was dissolved concerning all available H_2O_2 molecules.

In the bulk experiments, by fitting experimental data we obtained η_{H2O2} values 0.51, 0.585, and 0.60 for water thickness 7.54, 3.77, and 1.51 mm, respectively, at the gas flow rate 1 l/min. Figure 18a shows the solvation efficiency obtained in the H_2O_2 ES experiment with Q_w 200, 500, and 1000 µl/min, treatment time 1 min, at the gas flow rate 1 l/min. If we compare the bulk liquid experiment with H = 3.77 mm (500 µl of water) where η_{H2O2} = 0.585, with the ES experiment (Figure 18a), we can see that at 7.5 kV and Q_w = 500 µl/min, the solvation efficiency is also only around 0.5.

Preprints (www.preprints.org) | NOT PEER-REVIEWED | Posted: 1 December 2020 doi:10.20944/preprints202012.0025.v1

It does not mean that at 7.5 kV there is no contribution of microdroplets to the dissolved H_2O_2. In the ES experiments, the bulk is being formed gradually and the water is sprayed into the reactor gradually, while in the bulk experiments all the water is inside the reactor all the time since the start. The average time during the water could be exposed to the gaseous H_2O_2 in the ES experiment is only 1/2 of the treatment time of the bulk experiment. Thus, it is more reasonable to compare the solvation efficiency from the ES experiments with ½ of the solvation efficiency obtained in the bulk liquid experiments (Figure 18a). Thus, we assume that at 7.5 kV and 500 µl/min where η_{H2O2} ~ 0.5 (Figure 18a), the highest theoretical contribution of H_2O_2 solvation to the bulk liquid is about 0.29, i.e. 50%, from 0.58. This number is probably slightly higher at higher Q_w (faster bulk liquid formation), and slightly lower at lower Q_w.

We can see that the solvation to microdroplets (both flying and bottom) plays an important role since the parameter η_{H2O2} increases with an increasing V_a at all Q_w. The highest solvation efficiency approaching 100% was obtained at Q_w = 1000 µl/min. As we already discussed, the formation of big droplets and the formed bulk water inside the ES reactor is the fastest at the Q_w = 1000 µl/min, where the role of the sitting bottom droplets should be minimal. This seems to indicate that the solvation effect is mostly due to flying microdroplets. However, we must also consider the fact that η_{H2O2} depends on the total amount of flown water. More water can simply dissolve more H_2O_2.

To compare data obtained at different Q_w, it is necessary to normalize the solvation efficiency η_{H2O2} to the same flown water volume, e.g. to 1000 µl. Before this normalization, the H_2O_2 solvation in the ES experiment with Q_w of 200 µl/min (gas flow 1 l/min, treatment time 1 min) seems to be much less efficient than in the experiments with higher flow rates (Figure 18a). After this normalization (Figure 18b), however, the trend is the opposite: the highest normalized solvation efficiency occurs at Q_w = 200 µl/min. This indicates that the solvation into sitting bottom droplets plays a significant role at these lower Q_w, although we are not able to estimate its exact contribution from this normalized solvation efficiency.

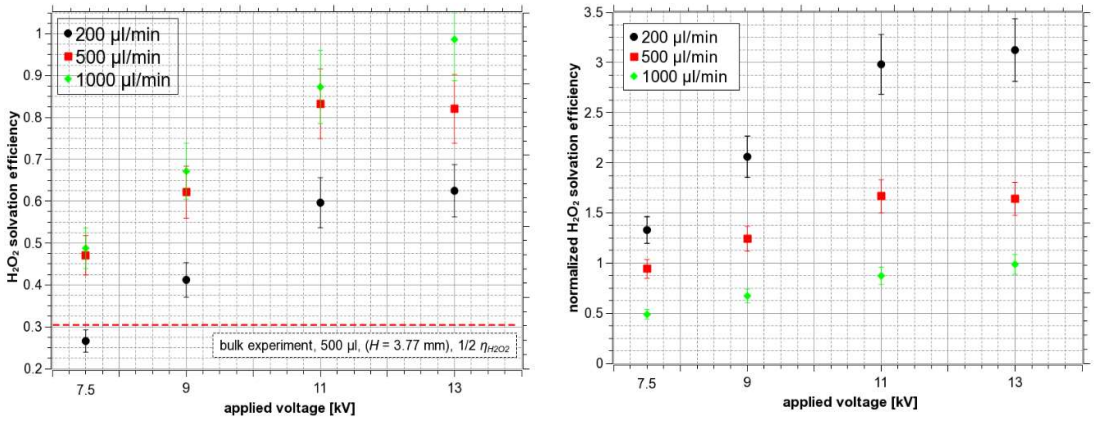

(**a**) (**b**)

Figure 18. Solvation efficiency and the solvation efficiency of H_2O_2 normalized to 1000 µl of water at a gas flow of 1 l/min (**a**) H_2O_2 solvation efficiency η_{H2O2} as a function of V_a (kV), treatment time 1 min, at different Q_w (µl/min); (**b**) comparison of the H_2O_2 solvation efficiency normalized to 1000 µl of water, both as a function of V_a.

5. Conclusions

Motivated by the increasing interest in plasma-liquid interactions and their biomedical, agriculture, and other applications, the objective of this article was to investigate the transport of the most typical air plasma reactive species (O_3 and H_2O_2) into water. We conducted solvation experiments with single O_3 and H_2O_2 species in the airflow at elevated concentrations and analyzed their transport into bulk water vs. electrosprayed aerosol microdroplets.

The gas-water interface surface area and the treatment (interaction) time are shown to be the key parameters of determining the amount of dissolved O_3 and H_2O_2 in the bulk water regardless of the water volume. The higher the gas flow rate of the incoming air with O_3 or H_2O_2 resulted in a lower amount of dissolved O_3 due to the insufficient interaction time. On the other hand, we detected slightly higher solvation of H_2O_2 thanks to more incident H_2O_2 molecules, despite their shorter interaction time.

The size distribution of the electrosprayed water microdroplets was measured by the Fast/HS camera imaging. The total surface area of water microdroplets increased with the increasing applied voltage and water flow rate. The dissolved O_3 and H_2O_2 also increased with increasing voltage and water flow rate, but the observed effect cannot be explained simply by the measured droplet size distribution and their total surface area. The limitation in the ES experiment is a very short lifetime (up to 9 ms only) of the generated flying microdroplets. In addition to the very short flying phase of the ES microdroplets, there are other phases of their total interaction time with O_3 and H_2O_2, such as microdroplets sitting at the reactor bottom (and walls) until they merge and form the bulk and the progressively forming bulk at the reactor bottom. All these phases of the water interaction with O_3 and H_2O_2 strongly contribute to the solvation of O_3 and H_2O_2 into ES water.

We confronted the experimental results with a simple theory. There is a good agreement between the experimental and theoretical results of the time evolution of the saturation degree of H_2O_2 and O_3 for different bulk water volumes (i.e. water depth). We got ~ 10^4 times more H_2O_2 than O_3 solvated in the water despite the 10^7 times larger Henry's law coefficient of H_2O_2 than that of O_3 because of the amount of gaseous H_2O_2 molecules next to the gas-water interface area was depleted to get higher H_2O_2 saturation in water.

For O_3, we had to consider the diffusion of dissolved O_3 molecules inside the liquid water that makes the characteristic saturation time longer than predicted by the simple theory. After taking the diffusion in the liquid into account, we get a reasonable agreement of the saturation time evolution with the experiment.

For O_3 solvation in electrosprayed microdroplets, we had to account for their lifetime, as well as their contribution to the total water volume depending on their size and abundance. We also accounted for the sitting bottom microdroplets that have a slightly lower surface-to-volume ratio, but a much longer interaction time compared to the flying ES microdroplets. Finally, we had to consider the merging bottom droplets that progressively form the bulk at the bottom of the ES reactor. All water flow rates indicate the key role of the water microdroplets (both flying and bottom) on the total solvation during the ES.

For highly soluble H_2O_2, on the contrary, we analyzed the solvation efficiency parameter, which determines how many of the total gaseous H_2O_2 molecules dissolve, concerning the available H_2O_2 molecules. Although the bulk liquid solvation is more significant than in the O_3 case, the role of the solvation in flying and especially bottom microdroplets is important, too.

In summary, we experimentally demonstrated and theoretically explained that Henry's law coefficient is not the only important parameter to determine the solvation of H_2O_2 and O_3 gaseous species into the water. Other experimental parameters, such as the gas-liquid interface surface area, gas flow rate, and the treatment time should be considered for the solvation in the bulk liquid. In the ES microdroplets, in addition to these parameters, the applied voltage and the water flow rate are important. The roles of these parameters on flying microdroplets, bottom microdroplets, and the formed bulk were established, although more detailed experimental/theoretical studies of these individual phenomena are needed in the future. These physical parameters enable us to control the solvation efficiency of H_2O_2 and O_3 gases into water bulk and electrospray. Our findings contribute to a better understanding of the solvation process of different gaseous species and can lead to optimization of the water sprays and other plasma-water interaction systems and their working conditions for multiple applications.

Author Contributions: M.E.H. run and processed the experiments with microdroplets by fast/HS camera, and the investigations of H_2O_2 and O_3 solvation into bulk and electrosprayed water, and wrote the first draft of the manuscript; M.J. contributed to the microdroplet visualization experiments and wrote the theoretical parts in

the results and discussion including the comparison of the experimental and theoretical results; Z.M. planned, organized and supervised the research, and reviewed and edited the manuscript. All authors have read and agreed to the published version of the manuscript.

Funding: This work was supported by Slovak Research and Development Agency APVV-17-0382, APVV-0134-12 and SK-PL-18-0090, Slovak Grant Agency VEGA 1/0419/18, and Comenius University grants UK/317/2020 and UK/325/2019.

Acknowledgments: We thank Dr. Piotr Terebun, Dr. Michal Kwiatkowski, and Prof. Joanna Pawlat from Lublin University of Technology, Poland, for enabling us HS camera measurements.

Conflicts of Interest: The authors declare no conflict of interest in publishing this manuscript.

References

1. Bruggeman, P.; Leys, C. Non-thermal plasmas in and in contact with liquids. *J. Phys. D. Appl. Phys.* **2009**, *42*, 053001. 10.1088/0022-3727/42/5/053001.
2. Rezaei, F.; Vanraes, P.; Nikiforov, A.; Morent, R.; De Geyter, N. Applications of Plasma-Liquid Systems: A Review. *Materials (Basel).* **2019**, *12*, 2751. 10.3390/ma12172751.
3. Bruggeman, P.J.; Kushner, M.J.; Locke, B.R.; Gardeniers, J.G.E.; Graham, W.G.; Graves, D.B.; Hofman-Caris, R.C.H.M.; Maric, D.; Reid, J.P.; Ceriani, E.; et al. Plasma-liquid interactions: A review and roadmap. *Plasma Sources Sci. Technol.* 2016, *25*. 10.1088/0963-0252/25/5/053002.
4. Locke, B.R.; Sato, M.; Sunka, P.; Hoffmann, M.R.; Chang, J.S. Electrohydraulic discharge and nonthermal plasma for water treatment. *Ind. Eng. Chem. Res.* 2006, *45*, 882–905. 10.1021/ie050981u.
5. Locke, B.R. Environmental Applications of Electrical Discharge Plasma with Liquid Water-- A Mini Review--. *Int. J. Plasma Environ. Sci. Technol.* **2012**, *6*.
6. *Plasma-Surface Interactions and Processing of Materials*; Auciello, O., Gras-Martí, A., Valles-Abarca, J.A., Flamm, D.., Ed.; Springer Netherlands, 1990; 10.1007/978-94-009-1946-4.
7. Chen, Q.; Li, J.; Li, Y. A review of plasma-liquid interactions for nanomaterial synthesis. *J. Phys. D. Appl. Phys.* **2015**, *48*, 424005. 10.1088/0022-3727/48/42/424005.
8. *Plasma for Bio-Decontamination, Medicine and Food Security*; Machala, Z., Hensel, K., Akishev, Y., Eds.; NATO Science for Peace and Security Series A: Chemistry and Biology; Springer Netherlands: Dordrecht, 2012; ISBN 978-94-007-2851-6. 10.1007/978-94-007-2852-3.
9. Von Woedtke, T.; Schmidt, A.; Bekeschus, S.; Wende, K.; Weltmann, K.D. Plasma medicine: A field of applied redox biology. *In Vivo (Brooklyn).* **2019**, *33*, 1011–1026. 10.21873/invivo.11570.
10. Vanraes, P.; Bogaerts, A. Plasma physics of liquids - A focused review. *Appl. Phys. Rev.* 2018, *5*, 031103. 10.1063/1.5020511.
11. Kong, M.G.; Kroesen, G.; Morfill, G.; Nosenko, T.; Shimizu, T.; van Dijk, J.; Zimmermann, J.L. Plasma medicine: an introductory review. *New J. Phys.* **2009**, *11*, 115012. 10.1088/1367-2630/11/11/115012.
12. Fridman, G.; Friedman, G.; Gutsol, A.; Shekhter, A.B.; Vasilets, V.N.; Fridman, A. Applied Plasma Medicine. *Plasma Process. Polym.* **2008**, *5*, 503–533. 10.1002/ppap.200700154.
13. Laroussi, M. Low-Temperature Plasmas for Medicine? *IEEE Trans. Plasma Sci.* **2009**, *37*, 714–725. 10.1109/TPS.2009.2017267.
14. Šimončicová, J.; Kryštofová, S.; Medvecká, V.; Ďurišová, K.; Kaliňáková, B. Technical applications of plasma treatments: current state and perspectives. *Appl. Microbiol. Biotechnol.* 2019, *103*, 5117–5129. 10.1007/s00253-019-09877-x.
15. Laroussi, M.; Kong, M.; Morfill, G.; Stolz, W. *Plasma medicine: Applications of low-temperature gas plasmas in medicine and biology*; Cambridge University Press, 2012; Vol. 9781107006; ISBN 9780511902598. 10.1017/CBO9780511902598.
16. Fridman, A.; Friedman, G. *Plasma Medicine*; John Wiley and Sons, 2013; ISBN 9780470689707. 10.1002/9781118437704.
17. Fridman, G.; Peddinghaus, M.; Balasubramanian, M.; Ayan, H.; Fridman, A.; Gutsol, A.; Brooks, A. Blood Coagulation and Living Tissue Sterilization by Floating-Electrode Dielectric Barrier Discharge in Air. *Plasma Chem. Plasma Process.* **2006**, *26*, 425–442. 10.1007/s11090-006-9024-4.
18. Dobrynin, D.; Fridman, G.; Friedman, G.; Fridman, A. Physical and biological mechanisms of direct plasma interaction with living tissue. *New J. Phys.* **2009**, *11*, 115020. 10.1088/1367-2630/11/11/115020.
19. Stoffels, E.; Kieft, I.E.; Sladek, R.E.J. Superficial treatment of mammalian cells using plasma needle. *J. Phys. D. Appl. Phys.* **2003**, *36*, 2908–2913. 10.1088/0022-3727/36/23/007.
20. Choi, J.; Mohamed, A.-A.H.; Kang, S.K.; Woo, K.C.; Kim, K.T.; Lee, J.K. 900-MHz Nonthermal Atmospheric Pressure Plasma Jet for Biomedical Applications. *Plasma Process. Polym.* **2010**, *7*, 258–263.

10.1002/ppap.200900079.

21. Lloyd, G.; Friedman, G.; Jafri, S.; Schultz, G.; Fridman, A.; Harding, K. Gas Plasma: Medical Uses and Developments in Wound Care. *Plasma Process. Polym.* **2010**, *7*, 194–211. 10.1002/ppap.200900097.
22. Kovalóvá, Z.; Zahoran, M.; Zahoranová, A.; Machala, Z. Streptococci biofilm decontamination on teeth by low-temperature air plasma of dc corona discharges. *J. Phys. D. Appl. Phys.* **2014**, *47*, 224014. 10.1088/0022-3727/47/22/224014.
23. Metelmann, H.R.; von Woedtke, T.; Weltmann, K.D. *Comprehensive clinical plasma medicine: Cold physical plasma for medical application*; Springer International Publishing, 2018; ISBN 9783319676272. 10.1007/978-3-319-67627-2.
24. Parvulescu, V.I.; Magureanu, M.; Lukes, P. *Plasma Chemistry and Catalysis in Gases and Liquids*; Parvulescu, V.I., Magureanu, M., Lukes, P., Eds.; Wiley-VCH Verlag GmbH & Co. KGaA: Weinheim, Germany, 2012; ISBN 9783527649525. 10.1002/9783527649525.
25. Puač, N.; Gherardi, M.; Shiratani, M. Plasma agriculture: A rapidly emerging field. *Plasma Process. Polym.* **2018**, *15*, 1700174. 10.1002/ppap.201700174.
26. Thirumdas, R.; Kothakota, A.; Annapure, U.; Siliveru, K.; Blundell, R.; Gatt, R.; Valdramidis, V.P. Plasma activated water (PAW): Chemistry, physico-chemical properties, applications in food and agriculture. *Trends Food Sci. Technol.* 2018, *77*, 21–31. 10.1016/j.tifs.2018.05.007.
27. Ebihara, K.; Mitsugi, F.; Ikegami, T.; Nakamura, N.; Hashimoto, Y.; Yamashita, Y.; Baba, S.; Stryczewska, H.D.; Pawlat, J.; Teii, S.; et al. Ozone-mist spray sterilization for pest control in agricultural management. In Proceedings of the EPJ Applied Physics; EDP Sciences, 2013; Vol. 61, p. 24318. 10.1051/epjap/2012120420.
28. Oehmigen, K.; Hähnel, M.; Brandenburg, R.; Wilke, C.; Weltmann, K.-D.; von Woedtke, T. The Role of Acidification for Antimicrobial Activity of Atmospheric Pressure Plasma in Liquids. *Plasma Process. Polym.* **2010**, *7*, 250–257. 10.1002/ppap.200900077.
29. Graves, D.B. The emerging role of reactive oxygen and nitrogen species in redox biology and some implications for plasma applications to medicine and biology. *J. Phys. D. Appl. Phys.* **2012**, *45*, 263001. 10.1088/0022-3727/45/26/263001.
30. Brisset, J.L.; Pawlat, J. Chemical Effects of Air Plasma Species on Aqueous Solutes in Direct and Delayed Exposure Modes: Discharge, Post-discharge and Plasma Activated Water. *Plasma Chem. Plasma Process.* 2016, *36*, 355–381. 10.1007/s11090-015-9653-6.
31. Machala, Z.; Tarabová, B.; Sersenová, D.; Janda, M.; Hensel, K. Chemical and antibacterial effects of plasma activated water: correlation with gaseous and aqueous reactive oxygen and nitrogen species, plasma sources and air flow conditions. *J. Phys. D. Appl. Phys.* **2019**, *52*, 034002. 10.1088/1361-6463/aae807.
32. Machala, Z.; Tarabova, B.; Hensel, K.; Spetlikova, E.; Sikurova, L.; Lukes, P. Formation of ROS and RNS in Water Electro-Sprayed through Transient Spark Discharge in Air and their Bactericidal Effects. *Plasma Process. Polym.* **2013**, *10*, 649–659. 10.1002/ppap.201200113.
33. Sander, R. Compilation of Henry's law coefficients (version 4.0) for water as solvent. *Atmos. Chem. Phys.* **2015**, *15*, 4399–4981. 10.5194/acp-15-4399-2015.
34. Stratton, G.R.; Bellona, C.L.; Dai, F.; Holsen, T.M.; Thagard, S.M. Plasma-based water treatment: Conception and application of a new general principle for reactor design. *Chem. Eng. J.* **2015**, *273*, 543–550. 10.1016/j.cej.2015.03.059.
35. Verlackt, C.C.W.; Van Boxem, W.; Bogaerts, A. Transport and accumulation of plasma generated species in aqueous solution. *Phys. Chem. Chem. Phys.* **2018**, *20*, 6845–6859. 10.1039/C7CP07593F.
36. Yusupov, M.; Neyts, E.C.; Simon, P.; Berdiyorov, G.; Snoeckx, R.; Van Duin, A.C.T.; Bogaerts, A. Reactive molecular dynamics simulations of oxygen species in a liquid water layer of interest for plasma medicine. *J. Phys. D. Appl. Phys.* **2014**, *47*. 10.1088/0022-3727/47/2/025205.
37. Kruszelnicki, J.; Lietz, A.M.; Kushner, M.J. Interaction between atmospheric pressure plasmas and liquid microdroplets* International Conference on Plasmas with Liquids (ICPL 2017) ed P Lukeš and K Koláček (Prague, Czech Republic), p 37.; 2017.
38. Kruszelnicki, J.; Lietz, A.M.; Kushner, M.J. Atmospheric pressure plasma activation of water droplets. *J. Phys. D. Appl. Phys.* **2019**, *52*, 355207. 10.1088/1361-6463/AB25DC.
39. Oinuma, G.; Nayak, G.; Du, Y.; Bruggeman, P.J. Controlled plasma-droplet interactions: A quantitative study of OH transfer in plasma-liquid interaction. *Plasma Sources Sci. Technol.* **2020**, *29*, 095002. 10.1088/1361-6595/aba988.
40. Burlica, R.; Grim, R.G.; Shih, K.-Y.; Balkwill, D.; Locke, B.R. Bacteria Inactivation Using Low Power Pulsed Gliding Arc Discharges with Water Spray. *Plasma Process. Polym.* **2010**, *7*, 640–649. 10.1002/ppap.200900183.

41. Kanev, I.L.; Mikheev, A.Y.; Shlyapnikov, Y.M.; Shlyapnikova, E.A.; Morozova, T.Y.; Morozov, V.N. Are Reactive Oxygen Species Generated in Electrospray at Low Currents? *Anal. Chem.* **2014**, *86*, 1511–1517. 10.1021/ac403129f.
42. Pyrgiotakis, G.; McDevitt, J.; Bordini, A.; Diaz, E.; Molina, R.; Watson, C.; Deloid, G.; Lenard, S.; Fix, N.; Mizuyama, Y.; et al. A chemical free, nanotechnology-based method for airborne bacterial inactivation using engineered water nanostructures. *Environ. Sci. Nano* **2014**, *1*, 15–26. 10.1039/c3en00007a.
43. Kovalova, Z.; Leroy, M.; Kirkpatrick, M.J.; Odic, E.; Machala, Z. Corona discharges with water electrospray for Escherichia coli biofilm eradication on a surface. *Bioelectrochemistry* **2016**, *112*, 91–99. 10.1016/j.bioelechem.2016.05.002.
44. Bosi, F.J.; Tampieri, F.; Marotta, E.; Bertani, R.; Pavarin, D.; Paradisi, C. Characterization and comparative evaluation of two atmospheric plasma sources for water treatment. *Plasma Process. Polym.* **2018**, *15*, 1700130. 10.1002/ppap.201700130.
45. Locke, B.R.; Shih, K.Y. Review of the methods to form hydrogen peroxide in electrical discharge plasma with liquid water. *Plasma Sources Sci. Technol.* 2011, *20*, 034006. 10.1088/0963-0252/20/3/034006.
46. Lukes, P.; Appleton, A.T.; Locke, B.R. Hydrogen Peroxide and Ozone Formation in Hybrid Gas-Liquid Electrical Discharge Reactors. *IEEE Trans. Ind. Appl.* **2004**, *40*, 60–67. 10.1109/TIA.2003.821799.
47. ARISTOVA NA, PISKAREV IM, IVANOVSKII AV, SELEMIR VD, SPIROV GM, S.S. Initiation of chemical reactions with an electric discharge in a solid dielectric-gas-liquid system. *Russ. J. Phys. Chem. A* **2004**, *78*, 1144–1148.
48. Winter, J.; Tresp, H.; Hammer, M.U.; Iseni, S.; Kupsch, S.; Schmidt-Bleker, A.; Wende, K.; Dünnbier, M.; Masur, K.; Weltmann, K.D.; et al. Tracking plasma generated H2O2 from gas into liquid phase and revealing its dominant impact on human skin cells. *J. Phys. D. Appl. Phys.* **2014**, *47*, 285401. 10.1088/0022-3727/47/28/285401.
49. Cloupeau, M.; Prunet-Foch, B. Electrohydrodynamic spraying functioning modes: a critical review. *J. Aerosol Sci.* **1994**, *25*, 1021–1036. 10.1016/0021-8502(94)90199-6.
50. Grace, J.M.; Marijnissen, J.C.M. A review of liquid atomization by electrical means. *J. Aerosol Sci.* **1994**, *25*, 1005–1019. 10.1016/0021-8502(94)90198-8.
51. Borra, J.P.; Ehouarn, P.; Boulaud, D. Electrohydrodynamic atomisation of water stabilised by glow discharge - Operating range and droplet properties. *J. Aerosol Sci.* **2004**, *35*, 1313–1332. 10.1016/j.jaerosci.2004.05.011.
52. Hayati, I.; Bailey, A.I.; Tadros, T.F. Investigations into the mechanisms of electrohydrodynamic spraying of liquids. I. Effect of electric field and the environment on pendant drops and factors affecting the formation of stable jets and atomization. *J. Colloid Interface Sci.* **1987**, *117*, 205–221. 10.1016/0021-9797(87)90185-8.
53. Pongrác, B.; Kim, H.H.; Janda, M.; Martišovitš, V.; Machala, Z. Fast imaging of intermittent electrospraying of water with positive corona discharge. *J. Phys. D. Appl. Phys.* **2014**, *47*, 315202. 10.1088/0022-3727/47/31/315202.
54. Jaworek, A.; Sobczyk, A.; Czech, T.; Krupa, A. Corona discharge in electrospraying. *J. Electrostat.* **2014**, *72*, 166–178. 10.1016/J.ELSTAT.2014.01.004.
55. Maguire, P.D.; Mahony, C.M.O.; Kelsey, C.P.; Bingham, A.J.; Montgomery, E.P.; Bennet, E.D.; Potts, H.E.; Rutherford, D.C.E.; McDowell, D.A.; Diver, D.A.; et al. Controlled microdroplet transport in an atmospheric pressure microplasma. *Appl. Phys. Lett.* **2015**, *106*, 224101. 10.1063/1.4922034.
56. Jaworek, A.; Ganán-Calvo, A.M.; Machala, Z. Low temperature plasmas and electrosprays. *J. Phys. D. Appl. Phys.* 2019, *52*, 233001. 10.1088/1361-6463/ab0fdb.
57. Borra, J.-P. Review on water electro-sprays and applications of charged drops with focus on the corona-assisted cone-jet mode for High Efficiency Air Filtration by wet electro-scrubbing of aerosols. *J. Aerosol Sci.* **2018**, *125*, 208–236. 10.1016/J.JAEROSCI.2018.04.005.
58. Stancampiano, A.; Gallingani, T.; Gherardi, M.; Machala, Z.; Maguire, P.; Colombo, V.; Pouvesle, J.-M.; Robert, E. Plasma and Aerosols: Challenges, Opportunities and Perspectives. *Appl. Sci.* **2019**, *9*, 3861. 10.3390/app9183861.
59. Eisenberg, G.M. Colorimetric Determination of Hydrogen Peroxide. *Ind. Eng. Chem. - Anal. Ed.* **1943**, *15*, 327–328. 10.1021/i560117a011.
60. Bader, H.; Hoigné, J. Determination of ozone in water by the indigo method. *Water Res.* **1981**, *15*, 449–456. 10.1016/0043-1354(81)90054-3.
61. Tarabová, B.; Lukeš, P.; Janda, M.; Hensel, K.; Šikurová, L.; Machala, Z. Specificity of detection methods of nitrites and ozone in aqueous solutions activated by air plasma. *Plasma Process. Polym.* **2018**, *15*, 1800030. 10.1002/ppap.201800030.

 doi:10.20944/preprints202012.0025.v1

62. Johnson, P.N.; Davis, R.A. Diffusivity of ozone in water. *J. Chem. Eng. Data* **1996**, *41*, 1485–1487. 10.1021/je9602125.